Draft version August 18, 2025
Typeset using LaTeX **twocolumn** style in AASTeX631

Secondary standards in the UKIRT faint standard fields

Marek Górski ,[1] Grzegorz Pietrzyński ,[1] Paulina Karczmarek ,[1] Gergely Hajdu ,[1] Mirosław Kicia ,[1] Mikołaj Kałuszyński ,[1] Joseph R. Eimer ,[2] Stephen A. Smee,[2] Bartłomiej Zgirski ,[3] Piotr Wielgórski ,[1] and Weronika Narloch [1]

[1] *Nicolaus Copernicus Astronomical Center, Polish Academy of Sciences, Bartycka 18, 00-716, Warsaw, Poland*
[2] *Johns Hopkins University, Department of Physics and Astronomy, 3701 San Martin Drive, Baltimore, MD 21218, USA*
[3] *Universidad de Concepción, Departamento de Astronomía, Casilla 160-C, Concepción, Chile*

ABSTRACT

We present precise J- and K-band photometric measurements for 128 near-infrared secondary standard stars, located in the 19 UKIRT/MKO primary faint standard fields. The data were collected over more than 50 nights, covering a decade of observations between 2008 and 2018 at the ESO La Silla Observatory, using the New Technology Telescope (NTT) equipped with the SOFI NIR camera. Presented magnitudes are calibrated onto the MKO photometric system. The J- and K-band magnitudes range from 10 to 15.8 mag, with median values of $\tilde{J} = 13.5$ and $\tilde{K} = 13$ mag. The selection process ensured high photometric quality, with a precision better than 0.01 mag for all stars. The catalog excludes stars with close neighbors, high proper motion, or variable stars. Using these fields for standardization can improve the precision and accuracy of photometric calibrations without incurring additional observational-time costs.

Keywords: methods: observational — techniques: photometric — infrared:stars

1. INTRODUCTION

The era of modern near-infrared (NIR) astronomical observations began in the 1960s with the development of highly sensitive PbS photometers. Unlike the previously used InSb detectors, the new cell could be cooled with liquid nitrogen to 77 K. This improvement reduced and stabilized the thermal radiation of the instrument, enabling brightness measurements up to 5 µm. At the same time, the photometric system was expanded with J-, K-, L- and M-bands, centered at approximately 1.3, 2.2, 3.6 and 5.0 µm, respectively (Johnson 1962).

Soon after, Johnson (1966) presented a list of J- and K-band measurements of 653 bright stars, setting up the first list of NIR standards. It is worth noting that NIR photometry was obtained in two different observatories – Catalina Station of the Lunar and Planetary Laboratory of the University of Arizona and in the Tonantzintla Observatory in Mexico – using two different photometers. The absolute calibration of this system is anchored to Vega, with a V-band magnitude of 0.03 and $V{-}J$ and $V{-}K$ colors of 0.01, which consequently yields a $J{-}K$ color of 0.

In the next decade, selected observatories began near-infrared observations with photometers based on PbS and InSb detectors. Often, each observatory had its own in-house set of standard stars, composed of a subsample of objects from the Johnson (1966) list and extended with additional bright stars. This list of observatory-specific standards was anchored using different approaches. The first list used in the South African Astronomical Observatory (SAAO) was published by Glass (1974) and was standardized each night with a subsample of roughly 20 stars from the Johnson (1966) list. This list was later improved and expanded by Carter (1990), who adjusted the zero points of the J- and K-band magnitudes so that the locus of the $V - K$ and $V - J$ relations against $B - V$ passed through the origin. In 1978, Frogel et al. published a list of 22 standard stars used by the Caltech/Tololo (CIT) observatories, which was complemented with fainter stars by Elias et al. (1982). The zero points of the CIT system were established by adopting 0.00 magnitudes and colors for Vega. A different approach was used at the

Corresponding author: Marek Górski
mgorski@camk.edu.pl

ESO La Silla observatory, where a set of 87 stars was calibrated to match the Vega 0.00 magnitude in the V-band, but the NIR zero points were shifted to match the solar energy distribution (Engels et al. 1981; Wamsteker 1981). The Mount Stromlo Observatory (MSO) system (Jones & Hyland 1982) was tied with the fundamental standard (HR3314) to the Glass (1974) measurements for this star. The MSO system provided the basis for the development of the Anglo-Australian Observatory (AAO) standard list (Allen & Cragg 1983), which was additionally composed of stars from the Glass (1974) and Frogel et al. (1978) lists. The AAO system was later refined as the Mount Stromlo and Siding Springs Observatory (MSSSO) system (McGregor 1994).

Although the different approaches used for the zero-point calibration of the described systems introduced only systematic shifts, it was already clear that comparing the brightness of stars between these systems is more complex. Despite the fact that all systems were based on the Johnson (1966) list, it could not be used as a common reference due to its insufficient accuracy. Furthermore, the lists of standards for the northern and southern hemispheres remained separate, and only a limited number of comparison stars were available. Moreover, those early lists contained systematic errors, and variable stars were present. At different observatories, the filters used had varying characteristics; they differed in effective wavelength, half-power width, and, in principle, tended to be too broad, often including atmospheric lines. This effect was further amplified by the unique characteristics of atmospheric transparency at different observatories. Finally, the detectors exhibited different spectral responses and deviations from linearity. Even if specific color-based transformations between systems were established, they would fail for particular stars with strong absorption lines or those that were heavily reddened. Despite the problems described above, it was possible to establish color transformations between the CIT and AAO systems (Elias et al. 1983), as well as between the ESO and SAAO/AAO systems (Bouchet et al. 1991).

In the 1990s, the introduction of NIR CCD arrays and the increasing size of telescope mirrors enabled measurements of fainter objects. However, it also revealed the need for fainter standards, as the existing list contained objects that were too bright for modern detectors, which became saturated under normal observing conditions. The SAAO list was extended with standards of brightness up to 10 magnitudes in the K-band by Carter & Meadows (1995), and Bouchet et al. (1991) introduced fainter stars to the ESO list. The CIT (Elias et al. 1982) system was the basis for a fainter standard list maintained at the 3.8 m UK Infrared Telescope (UKIRT) (Casali & Hawarden 1992), which was later adopted for calibration of 86 stars in the northern hemisphere of the ARNICA system (Hunt et al. 1998). Elias et al. (1982) list was also used as the basis for a new faint NIR standard system of the Las Campanas Observatory (LCO, or NICMOS) (Persson et al. 1998). The UKIRT fundamental list was refined by Hawarden et al. (2001) and in its final version it consists of 83 standard stars with K-band magnitudes ranging from 9.5 to 15 mag. Although the list was based on the early-type stars of the CIT list, the magnitudes and colors of these stars were corrected, which established the UKIRT "natural" system. In the following years those standards were used extensively at different observatories, including the ESO La Silla and Paranal observatories.

Soon after, significant progress was achieved in terms of standardization and homogenization of photometric systems. Tokunaga et al. (2002) specified a new set of NIR filters designed to maximize throughput while simultaneously minimizing sensitivity to atmospheric water vapor, reducing background noise, and improving photometric transformations and color dependence in the extinction coefficient. All NIR telescopes at the Mauna Kea Observatory and many other around the world were equipped with these new filter system (including UKIRT, NASA Infrared Telescope Facility, Canada-France-Hawaii Telescope, Keck, Gemini, Subaru, Anglo-Australian Observatory, Nordic Optical Telescope, Osservatorio Astrofisico di Arcetri, Telescopio Nazionale Galileo, and ESO), and it was recommended as the preferred NIR photometric system by the IAU Working Group on Infrared Photometry. The compilation of standard stars, calibrated in the new MKO system was prepared by Leggett et al. (2006), and is composed of 79 standards from the UKIRT list of Hawarden et al. (2001) and 42 stars from the LCO/NICMOS list (Persson et al. 1998).

At the same time, large NIR surveys began operating, covering large parts of the sky, including DENIS (Fouqué et al. 2000), UKIDSS (Lawrence et al. 2007) and 2MASS (Cohen et al. 2003; Skrutskie et al. 2006). This development opened the possibility of measuring the brightness of the program stars relative to the catalog magnitude of a given survey, provided that the catalog stars were present in the same field and the photometric systems were sufficiently similar. Based on the UKIDSS and VISTA surveys, Leggett et al. (2020) presented a list of 81 standard stars with a median K-band brightness of 17.5 mag, dedicated to 8-m class telescopes, and future extremely large 30- to 40-m class telescopes.

Notably, the existing lists of standards mainly consist of stars that are too bright and tend to saturate detectors. Additionally, standard stars with precise measurements are sparsely distributed (typically one per field), which either requires significant overhead to achieve the desired standardization precision or reduces precision to maintain low observational overheads.

These limitations were acknowledged and addressed by the authors during research conducted as part of the Araucaria Project, which crucially depends on the precision and accuracy of NIR photometry. The Araucaria Project (Araucaria Project et al. 2023) is an international collaboration dedicated to improving the cosmic distance scale using primary distance indicators, including Cepheids (Pietrzyński et al. 2002; Gieren et al. 2005; Zgirski et al. 2017), the tip of the red giant branch (Górski et al. 2018), carbon stars (Zgirski et al. 2021), RR Lyrae stars (Karczmarek et al. 2017), and late-type eclipsing binaries (Pietrzyński et al. 2019).

As part of this project, we have collected a substantial volume of high-quality data, which we have recently decided to publish and make available to the scientific community (Karczmarek et al. 2021). In this paper, we present a list of secondary standard stars, calibrated and selected based on 10 years of NIR observations, located in 19 UKIRT faint standards fields.

The paper is organized as follows. In Section 2 we describe the NIR observations and instrumental calibrations. Photometry and standarization are detailed in Sections 3 and 4, respectively. In Section 5, we outline the selection criteria. The results are discussed in Section 6. Appendix A presents the observing log and detailed data for all standard fields analyzed.

2. OBSERVATIONS AND INSTRUMENTAL CALIBRATIONS

The data were collected over more than 50 nights, covering a decade of observations between 2008 and 2018 at the ESO La Silla Observatory, using the New Technology Telescope (NTT) equipped with the SOFI NIR camera (Moorwood et al. 1998). Using the Large Field (LF) mode of the instrument, its field of view was $4.9' \times 4.9'$ with a pixel scale of $0.288''\,\mathrm{pix}^{-1}$. These observations were conducted as part of multiple ESO observing proposals dedicated to the study of Cepheids and eclipsing binaries in the Magellanic Clouds. The complete list of proposal IDs is provided in Table 1.

Table 1. ESO observing proposals used in this work.

ESO Proposal ID
190.D-0237(B)
095.D-0424(B)
190.D-0237(D)
092.D-0295(B)
090.D-0409(B)
084.D-0591(E)
084.D-0591(B)
094.D-0056(B)
099.D-0307(A)
0102.D-0590(B)
084.D-0640(B)
097.D-0151(A)
088.D-0447(B)
088.D-0401(B)
0102.D-0469(B)
096.D-0170(B)
092.D-0349(A)
082.D-0513(A)

In addition to the program stars, each night a set of 5 to 14 standard stars from the list of Hawarden et al. (2001) was observed to secure the calibration of the measurements into the standard system. In this paper only observations of the specific fields containing standard stars are analyzed. Table 3 in Appendix A reports on which standards were observed each night.

Observations were performed using the dithering technique, where five consecutive exposures of a given field were shifted in both axes by $20''$, relative to the previous position (`SEQ.OFFSETX.LIST: "0 20 0 -40 0"`, `SEQ.OFFSETY.LIST: "0 20 -40 0 40"`). The subintegration times (DIT) ranged from 1.2 to 10 seconds, depending on the brightness of the standard star and seeing conditions, with 2, 3, 4 or 6 NDITs per one dither position.

Instrumental calibrations were typically performed shortly after the observations were made; however, over the course of the decade, the calibrations adhered to the procedures outlined in Pietrzyński & Gieren (2002). Basic routines included bad pixel correction, cosmic rays removal, dark correction and flat fielding, incorporating the `special_flat.cl` IRAF procedure provided by ESO on the SOFI website. In denser fields, sky subtraction was performed with a two-step process using the `XDIMSUM` IRAF package. In the first step, the sky map was obtained by taking the median of all dithered positions. The preliminary map was then subtracted from each individual image, detected stars were masked, and a second background map was calculated. Finally, all images were corrected for the sky background and stacked into the final image. For sparse fields, only one-step sky subtraction was used.

3. PHOTOMETRY

Photometry was performed individually for all FITS files in the J- and K- bands, separately for each field, using a dedicated pipeline based on the DAOPHOT II software package (Stetson 1987). Measurements were obtained for a set of six apertures, ranging in diameter from $1''$ to $6''$, with the sky background estimated within a concentric annulus of $7''$ inner and $10''$ outer diameter. Although the results presented in this paper are based entirely on aperture photometry, PSF photometry was also performed for denser fields (FS014, FS017, FS035, FS121) to subtract neighboring stars and assess the accuracy of aperture photometry. In all cases, the corrections derived from PSF photometry remained below the reported photometric errors.

As a result, a set of photometric files corresponding to each FITS file was obtained, effectively creating a list of magnitudes for a given field at a specific observation date (epoch). The instrumental coordinates were transformed into the WCS coordinates by cross-referencing with the Gaia DR3 catalog (Gaia Collaboration et al. 2023). We note that coordinates presented in this paper were finally transformed to epoch 2000 using the AstroPy package (Astropy Collaboration et al. 2022), including proper motions if available from the Gaia query.

The resulting lists of stars for individual epochs (observing dates), along with their coordinates, instrumental magnitudes, and corresponding errors, were cross-matched, creating a time series of instrumental magnitudes for all stars in the field. In order to bring instrumental measurements in different epochs to the same reference level, we performed differential photometry. A key aspect of this procedure is to correctly select comparison stars and remove objects that show excess noise. For this purpose, we developed an iterative method comprising three main steps.

Step 1: Initial Estimation of RMS Using a Single Comparison Star. For each target star, we selected a single comparison star - typically the primary standard in the field. The differential magnitude was calculated for each epoch, and the root mean square (RMS) of these differences was calculated. This RMS was then compared with the formal photometric error reported by the DAOPHOT for the target star.

DAOPHOT computes the formal error by accounting for the photon noise of the star, the noise from the sky background, and the detector's readout noise. However, in our case, the contribution of the readout noise is not accurately included because we did not provided a map of the number of dither positions stacked within a single pixel. As a result, this leads to an underestimation of the error, particularly for fainter objects.

In contrast, the calculated RMS includes a broader set of noise sources: contributions from photon noise, sky background noise, and the detector readout noise of both the target star and the comparison stars. Additionally, it incorporates other noise sources, such as residual errors from flat-fielding and instrumental calibration, detector edge effects, and, if present, intrinsic stellar variability.

Step 2: Fitting the RMS – Error Relation. To approximate the relationship between the calculated RMS and the formal DAOPHOT error, we fit a function of the following form:

$$f(x) = \log_{10}\left(10^{2x} + a\right) + b, \tag{1}$$

where x is the DAOPHOT error and a and b are free parameters of the function, corresponding to the additional noise. The function (1) is fitted with a custom procedure. From the entire sample of stars, five stars were randomly selected and using a `curve_fit` procedure from the SciPy package (Virtanen et al. 2020), the parameters a and b were determined. This process is repeated multiple times (typically 10 times the number of stars, but no more than 1000 repetitions), and the final parameter values are taken as the median of a and b [1].

Step 3: Selection of Comparison Stars. Using the fitted function 1 we selected new comparison stars for each target star. A star is qualified as a valid comparison star if it does not exceed the corresponding value of the fitted function by more than 0.01 mag, and if its formal DAOPHOT error is below 0.04 mag. The differential magnitude correction is calculated separately for each comparison star, and the final magnitude is obtained as the weighted average, with weights based on the RMS from Step 1.

Steps 2 and 3 were repeated (II iteration), using the newly calculated RMS for both comparison star selection and weighting. In practice, this final iteration had a marginal effect on the corrected magnitudes, but was retained for consistency.

Figure 1 shows the calculated RMS versus the average DAOPHOT error for all stars in the exemplary field FS001.

[1] The described procedure is similar to RANSAC; however, in RANSAC, the optimal model is selected based on the maximum number of data points that fit the model (e.g., by excluding outliers using 3-sigma clipping). In our approach, evaluating the optimal parameters as the median is sufficient for the intended purpose, and applying the full RANSAC procedure would require modeling the residuals.

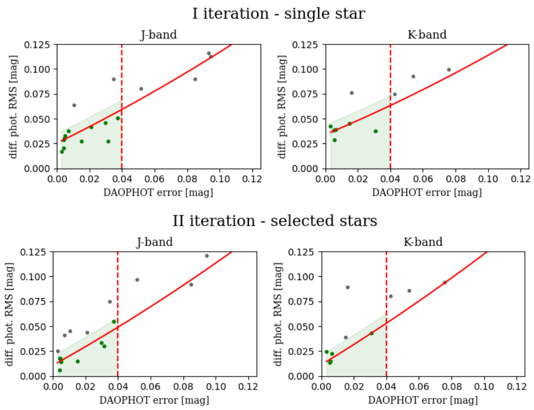

Figure 1. RMS versus the average DAOPHOT error for all stars in the exemplary field FS001. The upper panels display the results of the first iteration of the differential correction, while the lower panels present the results of the second iteration. The red solid lines represent the fitted models (eq. 1). Comparison stars (green points) were selected if their RMS value did not exceed the corresponding value of the fitted function by more than 0.01 mag, and if its formal DAOPHOT error was below 0.04 mag (dashed red vertical line). The green shaded area indicates the region where both criteria are satisfied.

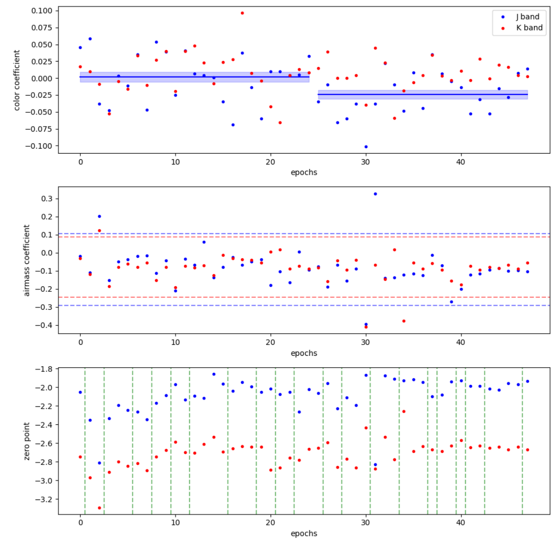

Figure 2. Equation 2 color-term coefficient (upper panel), airmass coefficient (middle panel), and zero-point (lower panel) values obtained for all nights (epochs) using the free-fit approach. Blue and red points represent values for the J- and K-band, respectively. The blue horizontal lines in the upper panel mark the average values of the J-band color-term coefficient with their corresponding uncertainty (blue shaded area) for the periods before 12 December 2013 and after 8 December 2014. Notably, the difference in the mean coefficient value reaches a significance level of 3 sigma. The dotted blue and red lines in the middle panel mark the 3σ range for the J and K bands, respectively. The green dashed vertical lines in the lower panel indicates epochs where consecutive observations were separated by more than one week.

The calculated RMS will be used to select secondary standards in Section 5, and differentially corrected instrumental magnitude time series are saved for further examination and analysis.

4. STANDARDIZATION

Standard stars observations analyzed in this work were originally used to transform J- and K-band instrumental magnitudes (lower case: j and k, respectively) of other objects onto the UKIRT standard system (upper case: J and K, respectively). Transformations were carried out following the relations (2).

$$\begin{aligned} J &= j + c_J(j-k) + k_J\chi + z_J \\ K &= k + c_K(j-k) + k_K\chi + z_K, \end{aligned} \tag{2}$$

where χ is the airmass at which the observations were executed and $j-k$ is the instrumental color of the star. A set of color-term coefficients (c_J, c_K), airmass coefficient (k_J, k_K) and zero points (z_J, z_K) were calculated each night using the least-squere method, adopting J and K from the Leggett et al. (2006) catalog. The values of the coefficients calculated for each night are presented in Figure 2.

Unfortunately, the uncertainty of the derived coefficients can be large, especially when an insufficient number of standard stars was observed on a given night. In fact, one could argue that the airmass coefficient should not vary more than 10% from night to night under photometric conditions (Burki et al. 1995), while the color coefficient should change only if significant modifications were made to the instrumental system. Based on Figure 2, we suspect that such a change may have occurred in 2014.

To verify this, we divided the entire observational period into two groups and calculated the mean value of the coefficient along with its uncertainty. We tested different separation dates, ensuring that no subsequent observations occurred within one month of the division date. Indeed, splitting the epochs into two groups, before 12 December 2013 and after 8 December 2014, resulted in the largest difference in the mean coefficient value, reaching a level of 3 sigma. This division also minimized the scatter within both separated groups for both filters. We note that we do not observe similar effect for airmass coefficient, neither there was a need for more than two groups for color coefficient.

In this paper, our objective is to improve the standardization process in two ways. First, we use the catalog of Leggett et al. (2006) as a source of standard magnitudes of the analyzed standard stars. Second, we fit a single value of the airmass coefficient for the entire 10-year observational period and allow only two values of the color coefficient, separated into two periods: before 12 December 2013 and after 8 December 2014, independently for both bands.

We solve these equations algebraically by constructing the design matrix of the form:

$$
\begin{bmatrix}
(j-k)_{1,1} & 0 & \chi_{1,1} & 1 & 0 & \dots & 0 \\
(j-k)_{2,1} & 0 & \chi_{2,1} & 1 & 0 & \dots & 0 \\
\vdots & \vdots & \vdots & \vdots & \vdots & \ddots & \vdots \\
(j-k)_{m,1} & 0 & \chi_{m,1} & 1 & 0 & \dots & 0 \\
0 & (j-k)_{1,2} & \chi_{1,2} & 0 & 1 & \dots & 0 \\
0 & (j-k)_{2,2} & \chi_{2,2} & 0 & 1 & \dots & 0 \\
\vdots & \vdots & \vdots & \vdots & \vdots & \ddots & \vdots \\
0 & (j-k)_{m,n} & \chi_{m,n} & 0 & 0 & \dots & 1
\end{bmatrix}
$$

where m denotes the ordinal number of the standard star observed on a given night and n represents the ordinal number of the night.

Figure 3 presents the zero-point values calculated using this method, and Table 2 reports their numerical values.

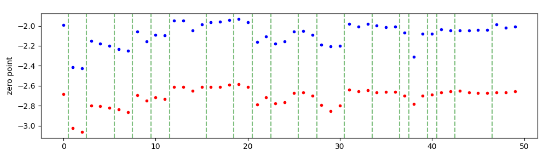

Figure 3. Equation 2 zero-points values obtained for all nights (epochs) using the general least-square fitting using a single value of the airmass coefficient for the entire 49 epochs observational period and two values of the color coefficient, separated into two periods: before 12 December 2013 and after 8 December 2014, for the J- and K-band (blue and red points, respectively). The green dashed vertical lines indicate epochs where consecutive observations were separated by more than one week. It can be noted that zero-point variations are much smaller compared to the free-fit results presented in Figure 2.

Finally, we applied Equation 2 to instrumental magnitudes to obtain standarized magnitudes for all stars in the fields, for each observing epoch.

5. SELECTION OF SECONDARY STANDARDS

Our goal was to prepare a catalog of selected secondary standards with the highest possible photometric quality while ensuring ease of use without accounting for any additional effects.

To select stars with the best photometry, we used the RMS calculated in Section 3 and the uncertainty of the mean value of the standardized magnitude from Section 4. Every star in the final list met the following conditions:

- The standardized J- and K-band magnitudes are measured in at least five epochs.
- The uncertainty of the average standardized magnitude is below 0.01 mag for both J- and K-band simultaneously. The uncertainty is calculated as $\sigma_{\bar{x}} = s \ / \ \sqrt{N}$, where s is the standard deviation and N is the number of epochs.
- The RMS of the differential photometry across all epochs is below 0.03 mag for both J- and K-band simultaneously.
- There is no excess of photometric noise in the J- and K-bands. This condition was applied using the same technique as described in Section 3: A star is excluded if its RMS value exceeds the corresponding value from the fitted relation of RMS versus the formal DAOPHOT error (Equation 1) by more than 0.02 mag.

We note that all rejected stars failed at least two of the four necessary conditions. Figure 4 visualizes the photometric selection criteria for stars in the exemplary field FS001.

With the preselected list of stars that meet the photometric conditions for all fields, we applied additional criteria:

- Stars were rejected if there was a neighboring star closer than 6”.
- The star’s parallax (ASTROQUERY GAIA `parallax`) must satisfy $\varpi/\sigma_\varpi > 1$, where ϖ is the parallax and σ_ϖ is its uncertainty.
- The proper motion of the star (ASTROQUERY GAIA `pmra` and `pmdec`) must not exceed 100 mas/year.
- No variability flag (ASTROQUERY GAIA `vari_classifier_result`) can be assigned to the star.

The steps listed above involved querying Gaia DR3 data (Gaia Collaboration et al. 2023).

Table 2. Equation 2 coefficients

epoch	date	J-band zero point	J rms	K-band zero point	K rms
(epochs: 0-49 airmass		a_J = -0.0774 ± 0.0048		a_K = -0.0786 ± 0.0057)	
(epochs: 0-27 color		c_J = -0.0157 ± 0.0052		c_K = 0.0011 ± 0.0063)	
0	2008-12-13	-1.990 ± 0.015	0.025	-2.682 ± 0.019	0.011
1	2009-11-5	-2.414 ± 0.013	0.017	-3.024 ± 0.016	0.013
2	2009-11-7	-2.424 ± 0.016	0.049	-3.065 ± 0.020	0.063
3	2009-12-2	-2.152 ± 0.013	0.015	-2.798 ± 0.016	0.023
4	2009-12-3	-2.177 ± 0.011	0.019	-2.805 ± 0.014	0.020
5	2009-12-4	-2.199 ± 0.011	0.032	-2.823 ± 0.013	0.026
6	2009-12-26	-2.231 ± 0.014	0.022	-2.838 ± 0.017	0.016
7	2009-12-28	-2.251 ± 0.013	0.017	-2.867 ± 0.016	0.045
8	2011-12-30	-2.059 ± 0.015	0.015	-2.694 ± 0.018	0.017
9	2011-12-31	-2.157 ± 0.014	0.042	-2.747 ± 0.017	0.031
10	2012-1-6	-2.092 ± 0.013	0.029	-2.714 ± 0.016	0.022
11	2012-1-7	-2.098 ± 0.013	0.032	-2.734 ± 0.016	0.027
12	2012-10-10	-1.949 ± 0.011	0.023	-2.609 ± 0.013	0.031
13	2012-10-11	-1.947 ± 0.011	0.022	-2.610 ± 0.014	0.035
14	2012-10-12	-2.045 ± 0.016	0.087	-2.650 ± 0.019	0.058
15	2012-10-13	-1.986 ± 0.028	0.000	-2.614 ± 0.035	0.000
16	2012-11-1	-1.964 ± 0.012	0.016	-2.611 ± 0.015	0.032
17	2012-11-2	-1.960 ± 0.012	0.022	-2.614 ± 0.014	0.028
18	2012-11-3	-1.940 ± 0.012	0.018	-2.593 ± 0.014	0.012
19	2012-11-15	-1.933 ± 0.010	0.025	-2.587 ± 0.013	0.028
20	2012-11-16	-1.965 ± 0.011	0.022	-2.613 ± 0.013	0.028
21	2013-8-24	-2.164 ± 0.015	0.016	-2.790 ± 0.019	0.042
22	2013-8-25	-2.108 ± 0.017	0.016	-2.715 ± 0.021	0.019
23	2013-11-26	-2.180 ± 0.011	0.017	-2.778 ± 0.013	0.021
24	2013-11-27	-2.159 ± 0.012	0.016	-2.768 ± 0.014	0.010
25	2013-11-28	-2.058 ± 0.011	0.033	-2.675 ± 0.013	0.016
26	2013-12-11	-2.049 ± 0.011	0.017	-2.665 ± 0.013	0.018
27	2013-12-12	-2.091 ± 0.011	0.027	-2.700 ± 0.013	0.018
(epochs: 27-49 color		c_J = -0.0362 ± 0.0034		c_K = -0.0131 ± 0.0041)	
28	2014-12-8	-2.1868 ± 0.0112	0.035	-2.7915 ± 0.0136	0.034
29	2014-12-9	-2.2046 ± 0.0122	0.030	-2.8518 ± 0.0151	0.116
30	2014-12-10	-2.2008 ± 0.0120	0.021	-2.7969 ± 0.0145	0.017
31	2015-9-26	-1.9787 ± 0.0116	0.020	-2.6394 ± 0.0139	0.014
32	2015-9-27	-2.0097 ± 0.0104	0.024	-2.6559 ± 0.0127	0.027
33	2015-9-28	-1.9783 ± 0.0138	0.010	-2.6463 ± 0.0169	0.067
34	2015-12-19	-1.9994 ± 0.0119	0.020	-2.6671 ± 0.0145	0.023
35	2015-12-20	-2.0112 ± 0.0118	0.021	-2.6621 ± 0.0143	0.017
36	2015-12-21	-2.0105 ± 0.0129	0.023	-2.6595 ± 0.0162	0.016
37	2016-6-10	-2.0690 ± 0.0176	0.012	-2.6975 ± 0.0215	0.002
38	2016-6-26	-2.3075 ± 0.0177	0.052	-2.7810 ± 0.0222	0.040
39	2016-6-27	-2.0787 ± 0.0118	0.031	-2.7013 ± 0.0142	0.014
40	2017-9-7	-2.0772 ± 0.0111	0.028	-2.6866 ± 0.0135	0.030
41	2017-9-21	-2.0376 ± 0.0122	0.019	-2.6656 ± 0.0149	0.020
42	2017-9-22	-2.0482 ± 0.0141	0.020	-2.6552 ± 0.0172	0.014
43	2018-11-18	-2.0475 ± 0.0116	0.019	-2.6530 ± 0.0141	0.024
44	2018-11-19	-2.0440 ± 0.0123	0.014	-2.6679 ± 0.0150	0.029
45	2018-11-20	-2.0385 ± 0.0113	0.021	-2.6731 ± 0.0138	0.031
46	2018-11-21	-2.0391 ± 0.0122	0.035	-2.6707 ± 0.0153	0.021
47	2018-12-26	-1.9877 ± 0.0108	0.013	-2.6678 ± 0.0132	0.026
48	2018-12-27	-2.0164 ± 0.0104	0.022	-2.6652 ± 0.0127	0.028
49	2018-12-28	-2.0098 ± 0.0113	0.021	-2.6571 ± 0.0137	0.024

6. RESULTS AND DISCUSSION

Based on the criteria described in the previous section, we prepared a catalog of 128 secondary standards in 19 UKIRT faint standard fields. Figure 5 shows the location of those fields in the sky.

In the Appendix A we provide detailed information for each field, with the Finding Chart with marked po-

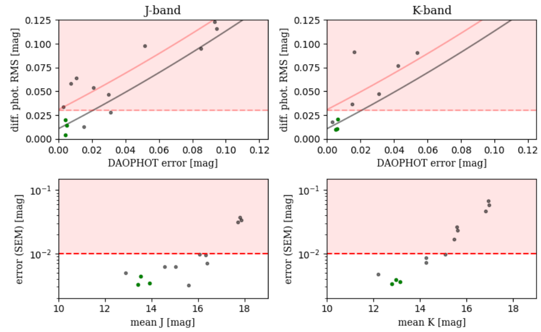

Figure 4. Photometric quality selection criteria visualized for stars in the fields FS001. Upper panels shows RMS versus the average DAOPHOT error for all stars in the exemplary field for J- and K-band. Red dashed horizontal line indicates RMS value of 0.03 mag, and shaded red color indicates rejection area. Black lines represent the fitted models (eq. 1) of RMS vs. DAOPHOT error relation used for excess noise estimation. Red solid line is shifted by 0.02 mag compared to the black line and indicates rejection condition. Lower panels show standard error of the mean (SEM) vs. mean value of the standardized J- and K-bands (left and right panels, respectively). Red dashed horizontal line indicates SEM value of 0.01 mag, and shaded red color indicates rejection area. Green points are stars that meet all the photometric conditions for secondary standards.

sitions of all secondary standards, color-magnitude diagrams of all secondary standards presented in this work, secondary standards for particular field (red points) and primary standard from the Hawarden et al. (2001) list for the J- and K-bands. Finally, for each field, we provide a table with the secondary standard assigned name, Gaia IDs, RA/Dec coordinates for epoch 2000, J- and K-bands magnitudes with corresponding uncertainty. The listed J and K magnitudes represent the mean values calculated across all available epochs, while the associated errors correspond to the standard error of the mean.

All of these products are also available on the Araucaria Project website (araucaria.camk.edu.pl) in additional formats.

6.1. *Re-standarization of the primary standards*

The J- and K-band magnitudes presented in this paper were transformed into the MKO system using Equation 2 and using coefficients from Table 2. A comparison between the transformed magnitudes of the primary standards and the catalog values provided by (Leggett et al. 2006) serves as a basic consistency check for the procedure (Figure 6). The average difference across all points is consistent with zero within the calculated errors of the mean. The small values of the Pearson correlation coefficient (R) suggest that there is no significant relation between the residuals and color or brightness. The average errors for the catalog data ($\sigma_{L06,J} = 0.009$, $\sigma_{L06,K} = 0.010$) and the average errors of re-standardized magnitudes presented in this study ($\sigma_{L06,J} = 0.006$, $\sigma_{L06,K} = 0.005$) are consistent with the observed scatter in the J-band. However, for the K-band, the scatter is approximately twice as large, which may indicate an underestimation of the errors provided by (Leggett et al. 2006), calculated in this work, or could suggest a difference between the MKO and NTT/SOFI photometric systems.

6.2. *Comparison with 2MASS*

In this subsection, we compare our data (J and K) with the magnitudes of the 2MASS catalog (J_{2MASS} and K_{2MASS}). Figure 7 presents the magnitude differences as a function of $J - K$ color and magnitude. In both bands, a systematic shift in magnitudes is observed, with a small but noticeable color dependence in the J-band. While the spread of differences in the J-band remains uniform across the entire magnitude range, in the K-band, it increases for magnitudes fainter than 13.5.

Leggett et al. (2006) provide coefficients for the color-based transformation between the MKO and 2MASS systems in their Table 4. Using a least-squares method, we derived transformation coefficients based on our data. The slope and zero-point for the J-band are consistent with the values reported by Leggett et al. (2006) within the fitting uncertainties. However, for the K-band, the slope of the relation has the opposite sign when all data points are considered. Nevertheless, the slope remains statistically consistent with zero within the uncertainties of the fit. This is a consequence of the relatively large photometric scatter for fainter sources ($K > 13.5$), which limits the precision of the derived transformation coefficients. When limiting the data set to objects with a smaller scatter (K-band magnitudes brighter than 13.5), the resulting slope and zero-point agree with the values from Leggett et al. (2006), and are given by:

$$J - J_{\mathrm{2MASS}} = (-0.080 \pm 0.011) \cdot (J - K) - (0.012 \pm 0.007),$$
$$K - K_{\mathrm{2MASS}} = (-0.021 \pm 0.010) \cdot (J - K) - (0.011 \pm 0.006).$$

6.3. *Deriving transformation coefficients with alternative approaches*

In Section 4, we derived the transformation coefficients of the photometric system by allowing only a single airmass coefficient and two color coefficients per band across all epochs.

If, instead of this procedure, we allow these coefficients to be fitted individually for each night, the average mag-

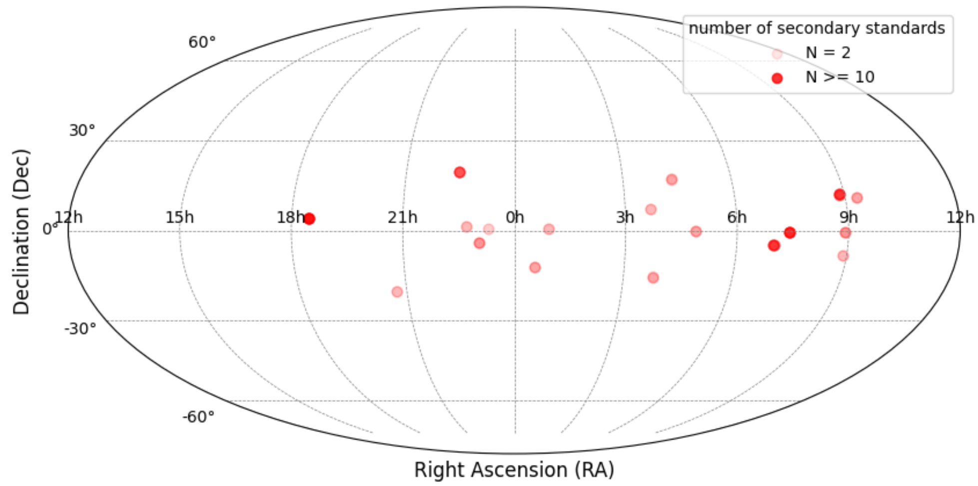

Figure 5. Location of the 20 UKIRT faint standard fields with secondary standards defined in this work. The sky map in RA/Dec Coordinates is in the Mollweide Projection. The intensity of the color of the points indicates the number of secondary standards in the field.

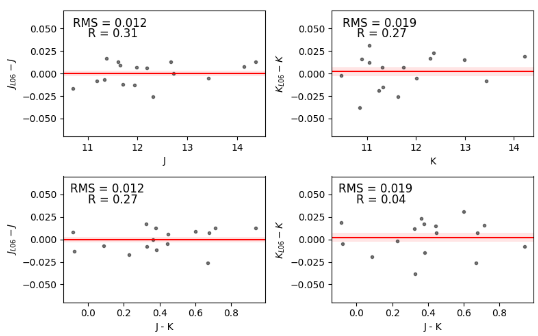

Figure 6. The difference between the catalog values of the primary standards (J_{L06}, K_{L06}) and the mean values calculated in this work (J and K). The catalog values are from Leggett et al. (2006). The differences are plotted against magnitudes (upper panels) and $J-K$ color (lower panels). The red horizontal line indicates the mean value of all points, and the red shaded area represents the error of the mean. The Pearson correlation coefficient (R) and standard deviation (RMS) of the residuals are also reported.

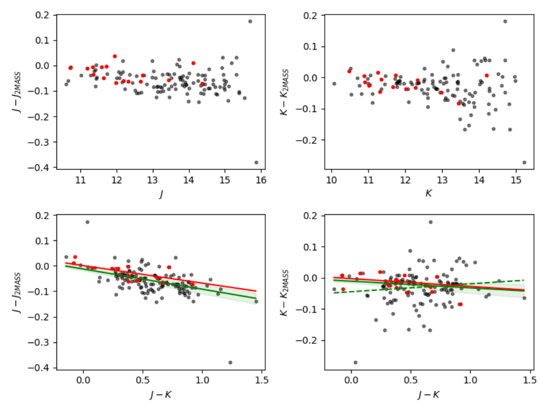

Figure 7. The difference between the magnitudes obtained in this work (J and K) and the 2MASS catalog values ($J_{\rm 2MASS}$ and $K_{\rm 2MASS}$). The upper panels show the magnitude differences as a function of magnitude, while the lower panels present them as a function of $J-K$ color. Red points represent primary standards, and black points correspond to secondary standards. The red solid lines in the lower panels indicate the color-based transformation between the MKO and 2MASS systems, as provided by Leggett et al. (2006). The green solid lines represent the transformations derived in this study. The K-band transformation was obtained by fitting a linear relation to objects brighter than 13.5 mag in the K-band. The green dashed line illustrates the transformation when all data points are included.

nitudes of the secondary standards remain virtually the same. However, the spread of magnitudes from night to night increases by 30%. As a result, the estimated uncertainty of the calculated average magnitudes is larger.

Additionally, we explored other coefficients combining procedures, such as grouping the airmass (and color) coefficients by month or by observing run. In all cases of combining multiple epochs, the resulting spread in magnitudes was significantly smaller than in the free-fit procedure. For consistency and clarity, we ultimately decided to adopt the procedure with one airmass and two color coefficients per band.

6.4. *Calibration of secondary standards relative to the primary standard*

In this work, we chose to calculate the magnitudes of all secondary standards separately, using calibration coefficients derived for each individual night.

An alternative approach would be to calibrate the brightness of secondary standards based on the brightness of the primary standard in a given field, accounting for instrumental magnitude differences, and applying a color correction. Although this method could improve statistical accuracy for some limited number of objects by roughly 0.001 mag, it would also introduce a systematic error for all stars in the field, comparable to the statistical uncertainty of the primary standard's brightness statistical uncertainty.

7. SUMMARY AND CONCLUSIONS

We presented a catalog of 128 secondary standard stars located in 19 UKIRT/MKO faint standard fields, based on 10 years of Araucaria Project observations using the NTT telescope equipped with the SOFI NIR camera. The average J- and K-band magnitudes of these stars are calibrated to the MKO photometric system of Leggett et al. (2006). The magnitudes range from 10 to 15.8, with medians of $\tilde{J} = 13.5$ and $\tilde{K} = 13$. The uncertainty in the brightness measurements is less than 0.01 mag for all stars. The $J - K$ colors of the secondary standards range from -0.07 to 1.4, with a median value of 0.53 mag. The number of newly defined secondary standards per field varies from 1 to 22, with fields FS121, FS035, and FS014 containing more than 10 stars each. Our results suggest that using these fields for standardization can improve the precision and accuracy of photometric calibrations without incurring additional observational-time costs.

The research leading to these results has received funding from the European Research Council (ERC) under the European Union's Horizon 2020 research and innovation program (grant agreement No. 951549). We acknowledge the contribution of present and former collaborators and members of the Araucaria Project, whose collective effort made this database possible.

Facilities: NTT

Software: astropy (Astropy Collaboration et al. 2022), astroquery, DAOPHOT, IRAF

REFERENCES

Allen, D. A., & Cragg, T. A. 1983, MNRAS, 203, 777, doi: 10.1093/mnras/203.3.777

Araucaria Project, T., :, Pietrzyński, G., et al. 2023, arXiv e-prints, arXiv:2305.17247, doi: 10.48550/arXiv.2305.17247

Astropy Collaboration, Price-Whelan, A. M., Lim, P. L., et al. 2022, ApJ, 935, 167, doi: 10.3847/1538-4357/ac7c74

Bouchet, P., Manfroid, J., & Schmider, F. X. 1991, A&AS, 91, 409

Burki, G., Rufener, F., Burnet, M., et al. 1995, A&AS, 112, 383

Carter, B. S. 1990, MNRAS, 242, 1, doi: 10.1093/mnras/242.1.1

Carter, B. S., & Meadows, V. S. 1995, MNRAS, 276, 734, doi: 10.1093/mnras/276.3.734

Casali, M., & Hawarden, T. 1992, JCMT-UKIRT Newsletter, 33

Cohen, M., Wheaton, W. A., & Megeath, S. T. 2003, AJ, 126, 1090, doi: 10.1086/376474

Elias, J. H., Frogel, J. A., Hyland, A. R., & Jones, T. J. 1983, AJ, 88, 1027, doi: 10.1086/113388

Elias, J. H., Frogel, J. A., Matthews, K., & Neugebauer, G. 1982, AJ, 87, 1029, doi: 10.1086/113185

Engels, D., Sherwood, W. A., Wamsteker, W., & Schultz, G. V. 1981, A&AS, 45, 5

Fouqué, P., Chevallier, L., Cohen, M., et al. 2000, A&AS, 141, 313, doi: 10.1051/aas:2000123

Frogel, J. A., Persson, S. E., Aaronson, M., & Matthews, K. 1978, ApJ, 220, 75, doi: 10.1086/155883

Gaia Collaboration, Vallenari, A., Brown, A. G. A., et al. 2023, A&A, 674, A1, doi: 10.1051/0004-6361/202243940

Gieren, W., Pietrzyński, G., Soszyński, I., et al. 2005, ApJ, 628, 695, doi: 10.1086/430903

Glass, I. S. 1974, MNRAS, 168, 249, doi: 10.1093/mnras/168.2.249

Górski, M., Pietrzyński, G., Gieren, W., et al. 2018, AJ, 156, 278, doi: 10.3847/1538-3881/aaeacb

Hawarden, T. G., Leggett, S. K., Letawsky, M. B., Ballantyne, D. R., & Casali, M. M. 2001, MNRAS, 325, 563, doi: 10.1046/j.1365-8711.2001.04460.x

Hunt, L. K., Mannucci, F., Testi, L., et al. 1998, AJ, 115, 2594, doi: 10.1086/300349

Johnson, H. L. 1962, ApJ, 135, 69, doi: 10.1086/147248

—. 1966, ApJ, 143, 187, doi: 10.1086/148489

Jones, T. J., & Hyland, A. R. 1982, MNRAS, 200, 509, doi: 10.1093/mnras/200.3.509

Karczmarek, P., Pietrzyński, G., Górski, M., Gieren, W., & Bersier, D. 2017, AJ, 154, 263, doi: 10.3847/1538-3881/aa9574

Karczmarek, P., Pietrzyński, G., Gieren, W., et al. 2021, ApJS, 253, 42, doi: 10.3847/1538-4365/abdf60

Lawrence, A., Warren, S. J., Almaini, O., et al. 2007, MNRAS, 379, 1599, doi: 10.1111/j.1365-2966.2007.12040.x

Leggett, S. K., Cross, N. J. G., & Hambly, N. C. 2020, MNRAS, 493, 2568, doi: 10.1093/mnras/staa310

Leggett, S. K., Currie, M. J., Varricatt, W. P., et al. 2006, MNRAS, 373, 781, doi: 10.1111/j.1365-2966.2006.11069.x

McGregor, P. J. 1994, PASP, 106, 508, doi: 10.1086/133406

Moorwood, A., Cuby, J. G., & Lidman, C. 1998, The Messenger, 91, 9

Persson, S. E., Murphy, D. C., Krzeminski, W., Roth, M., & Rieke, M. J. 1998, AJ, 116, 2475, doi: 10.1086/300607

Pietrzyński, G., & Gieren, W. 2002, AJ, 124, 2633, doi: 10.1086/344075

Pietrzyński, G., Gieren, W., Fouqué, P., & Pont, F. 2002, AJ, 123, 789, doi: 10.1086/338645

Pietrzyński, G., Graczyk, D., Gallenne, A., et al. 2019, Nature, 567, 200, doi: 10.1038/s41586-019-0999-4

Skrutskie, M. F., Cutri, R. M., Stiening, R., et al. 2006, AJ, 131, 1163, doi: 10.1086/498708

Stetson, P. B. 1987, PASP, 99, 191, doi: 10.1086/131977

Tokunaga, A. T., Simons, D. A., & Vacca, W. D. 2002, PASP, 114, 180, doi: 10.1086/338545

Virtanen, P., Gommers, R., Oliphant, T. E., et al. 2020, Nature Methods, 17, 261, doi: 10.1038/s41592-019-0686-2

Wamsteker, W. 1981, A&A, 97, 329

Zgirski, B., Gieren, W., Pietrzyński, G., et al. 2017, ApJ, 847, 88, doi: 10.3847/1538-4357/aa88c4

Zgirski, B., Pietrzyński, G., Gieren, W., et al. 2021, ApJ, 916, 19, doi: 10.3847/1538-4357/ac04b2

APPENDIX

A. OBSERVATION LOG AND INDIVIDUAL SECONDARY STANDARDS FIELDS

In the Appendix we report which standards were observed each night (Table 3) and provide detailed information for each of the 19 standard star fields. Finding charts are included, showing the positions of the primary standard (blue circle) and secondary standards (red circles) along with their names.

Color-magnitude diagrams are presented for the J- and K-bands vs. the J-K color. In each diagram, all secondary standards defined in this work across all fields are shown as black dots, while the primary standard and the secondary standards for the given field are represented as blue and red dots, respectively. Finally, for each field, we provide a table containing the names, RA/Dec coordinates (epoch 2000), J- and K-band magnitudes standardized to the MKO system, along with their corresponding uncertainties and their GAIA IDs. The primary standard is not shown for FS018 and FS124. In the case of FS018, the star is saturated in our observations, and no reliable photometry could be obtained due to observational limitations. The primary standard for FS124 was excluded from the final sample because of its high proper motion.

Table 3. Observation log of UKIRT standard stars. "X" indicates that the respective standard star was observed on that night.

Date	FS001	FS002	FS011	FS014	FS015	FS017	FS018	FS030	FS034	FS035	FS110	FS112	FS114	FS121	FS124	FS126	FS152	FS153	FS154
2008-12-13	X							X			X		X						
2009-11-05								X	X					X					X
2009-11-06	X								X										X
2009-11-07	X								X										X
2009-12-02					X				X		X		X						
2009-12-03	X			X	X				X				X						
2009-12-04	X				X	X			X		X			X					
2009-12-26		X		X	X														
2009-12-28				X	X														
2011-12-30			X				X					X	X	X	X				
2011-12-31					X		X				X	X	X	X	X				
2012-01-06						X								X	X	X			
2012-01-07							X				X	X	X			X			
2012-10-10		X								X	X	X	X				X		X
2012-10-11	X	X								X		X	X				X		X
2012-10-12																	X		
2012-10-13										X									
2012-11-01	X					X	X							X	X		X	X	X
2012-11-02	X	X									X	X			X	X	X	X	X
2012-11-03	X										X			X		X	X	X	
2012-11-15	X	X	X	X					X			X				X	X	X	
2012-11-16	X			X					X			X	X				X		X
2013-08-24													X						
2013-08-25									X	X									
2013-11-26	X			X	X	X					X		X	X					
2013-11-27				X		X							X	X					
2013-11-28	X		X	X	X	X					X		X	X	X				
2013-12-11	X						X				X		X	X	X	X		X	
2013-12-12	X						X						X	X	X	X		X	
2014-12-08	X	X	X	X					X		X	X	X						
2014-12-09		X	X						X			X	X						
2014-12-10		X	X	X		X						X	X	X					
2015-01-04	X										X		X					X	
2015-01-06												X	X					X	
2015-09-26	X	X		X					X				X		X				
2015-09-27	X		X						X	X		X	X				X	X	
2015-09-28									X	X			X					X	
2015-12-19					X			X					X		X	X			
2015-12-20			X		X							X	X	X		X		X	X
2015-12-21								X						X	X	X		X	X
2016-06-10					X		X												
2016-06-26								X										X	
2016-06-27									X										
2017-09-07								X	X		X							X	
2017-09-21		X							X				X						
2017-09-22									X				X						
2017-09-23									X										
2018-11-18			X	X			X		X			X		X			X		
2018-11-19			X				X							X	X	X		X	
2018-11-20			X					X				X			X		X		
2018-11-21				X				X									X	X	X
2018-12-26				X			X	X				X		X	X				
2018-12-27	X		X		X			X				X			X			X	
2018-12-28	X		X	X	X		X					X		X	X	X		X	

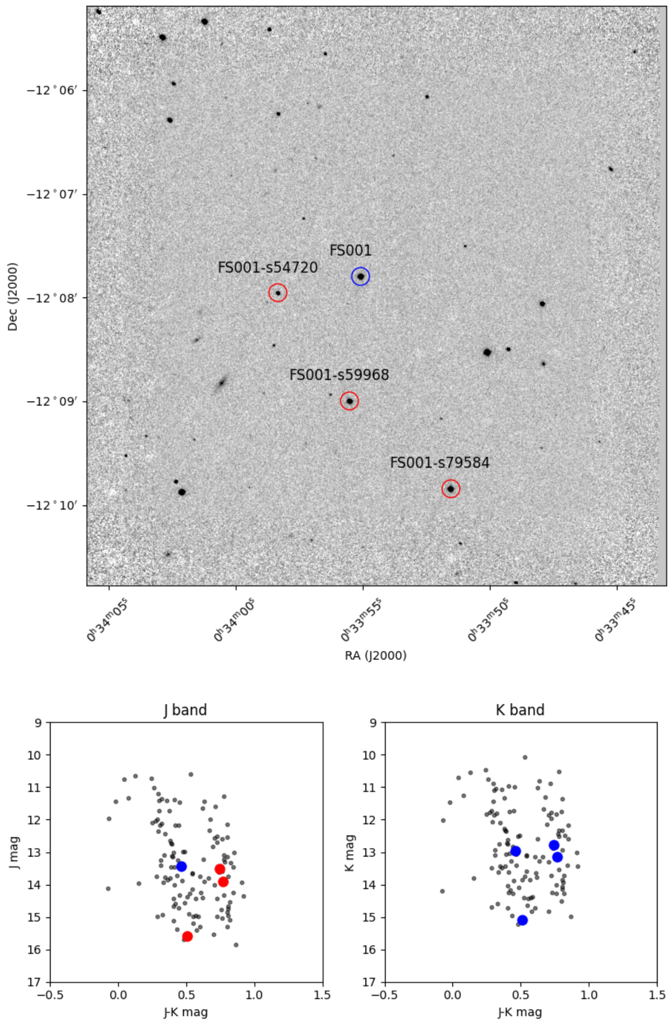

Figure 8. FS001 field finding chart and color-magnitude diagrams

Table 4. FS001

name	ra	dec	J	err J	epochs J	K	err K	epochs K	GAIA id
FS001	0:33:54.46	-12:07:58.78	13.432	0.003	17	12.969	0.004	17	2375647158466154112
FS001-s79584	0:33:51.05	-12:10:03.71	13.524	0.004	14	12.779	0.003	14	2375643688132579584
FS001-s59968	0:33:55.04	-12:09:13.14	13.915	0.003	17	13.146	0.004	17	2375643821276259968
FS001-s54720	0:33:57.86	-12:08:10.88	15.594	0.003	17	15.085	0.010	17	2375644203528654720

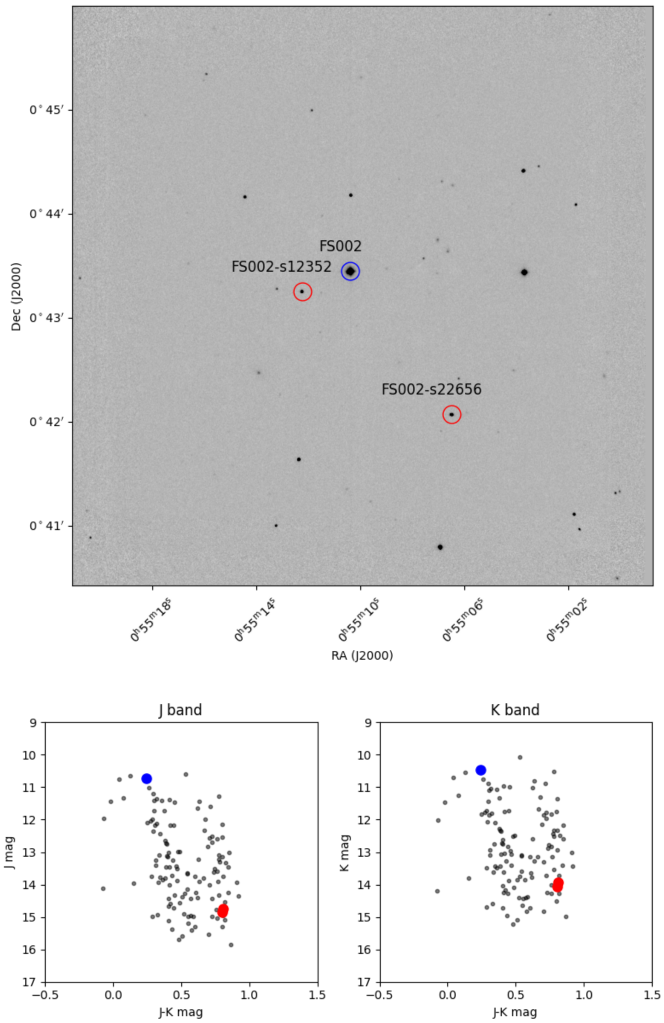

Figure 9. FS002 field finding chart and color-magnitude diagrams

Table 5. FS002

name	ra	dec	J	err J	epochs J	K	err K	epochs K	GAIA id
FS002	0:55:09.91	0:43:12.92	10.716	0.003	7	10.472	0.004	7	2537314812728975744
FS002-s22656	0:55:06.00	0:41:50.29	14.746	0.006	7	13.936	0.006	7	2537314675290022656
FS002-s12352	0:55:11.75	0:43:01.25	14.862	0.006	7	14.059	0.005	7	2537314808433812352

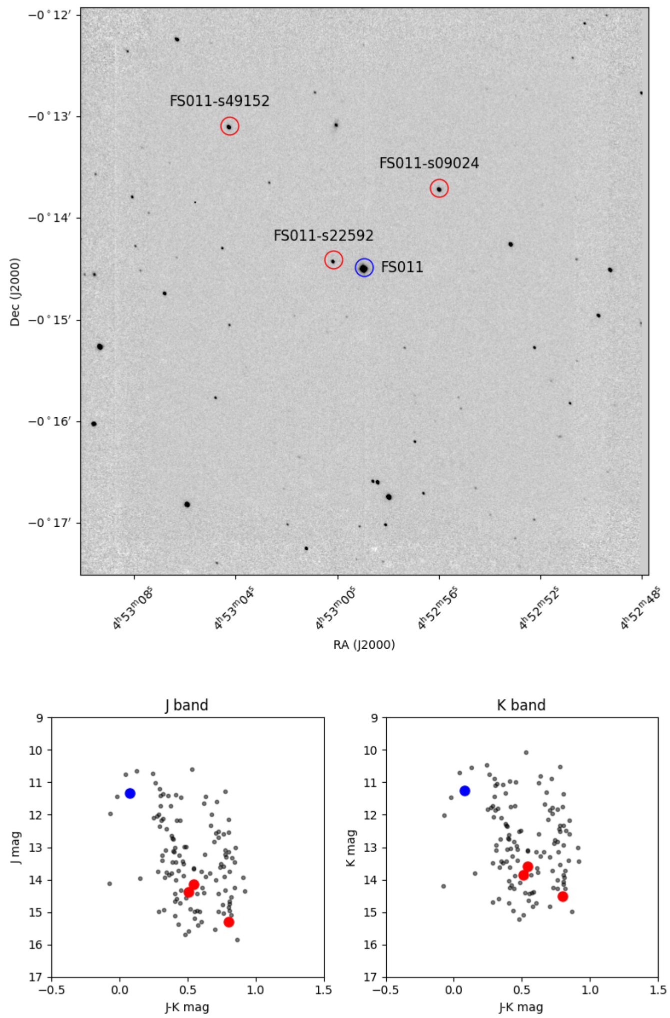

Figure 10. FS011 field finding chart and color-magnitude diagrams

Table 6. FS011

name	ra	dec	J	err J	epochs J	K	err K	epochs K	GAIA id
FS011	4:52:58.86	-0:14:41.17	11.336	0.005	10	11.260	0.004	10	3226810514329499648
FS011-s09024	4:52:55.88	-0:13:54.39	14.130	0.010	10	13.585	0.010	10	3226810720487809024
FS011-s49152	4:53:04.16	-0:13:17.76	14.373	0.008	9	13.865	0.006	9	3226810651768449152
FS011-s22592	4:53:00.06	-0:14:36.98	15.309	0.009	10	14.510	0.009	10	3226810510033822592

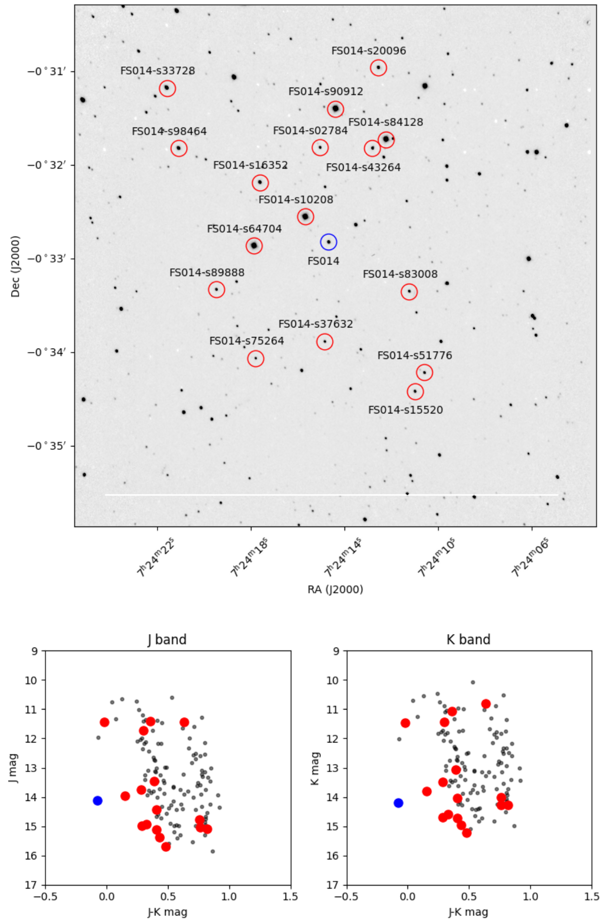

Figure 11. FS014 field finding chart and color-magnitude diagrams

Table 7. FS014

name	ra	dec	J	err J	epochs J	K	err K	epochs K	GAIA id
FS014-s90912	7:24:14.08	-0:31:38.68	11.442	0.007	13	10.808	0.007	13	3110405355740790912
FS014-s10208	7:24:15.38	-0:32:47.84	11.443	0.007	13	11.463	0.005	13	3110405183942110208
FS014-s64704	7:24:17.57	-0:33:06.18	11.415	0.006	13	11.055	0.005	13	3110404428027864704
FS014-s84128	7:24:11.93	-0:31:58.12	11.731	0.009	13	11.430	0.006	13	3110405252661584128
FS014-s33728	7:24:21.29	-0:31:25.28	13.462	0.007	13	13.072	0.006	13	3110405321381033728
FS014-s98464	7:24:20.78	-0:32:03.99	13.760	0.007	13	13.475	0.007	13	3110404565466798464
FS014-s16352	7:24:17.32	-0:32:25.83	13.957	0.007	13	13.805	0.008	13	3110405287021316352
FS014	7:24:14.37	-0:33:04.16	14.120	0.006	13	14.195	0.005	13	3110404393668131712
FS014-s20096	7:24:12.25	-0:31:12.40	14.441	0.008	13	14.035	0.010	13	3110405561899220096
FS014-s43264	7:24:12.51	-0:32:03.95	14.776	0.009	13	14.015	0.007	13	3110405248362843264
FS014-s89888	7:24:19.19	-0:33:34.35	15.036	0.006	13	14.272	0.006	13	3110404359308389888
FS014-s83008	7:24:10.93	-0:33:35.80	14.979	0.008	13	14.693	0.009	13	3110381681881083008
FS014-s15520	7:24:10.70	-0:34:39.83	14.929	0.007	13	14.602	0.008	13	3110380891607115520
FS014-s02784	7:24:14.74	-0:32:03.54	15.114	0.006	13	14.709	0.010	13	3110405183942102784
FS014-s51776	7:24:10.30	-0:34:28.00	15.094	0.006	13	14.276	0.010	13	3110380887308251776
FS014-s37632	7:24:14.54	-0:34:07.91	15.388	0.008	13	14.955	0.009	13	3110380925966837632
FS014-s75264	7:24:17.49	-0:34:18.50	15.696	0.010	13	15.216	0.007	13	3110404324950075264

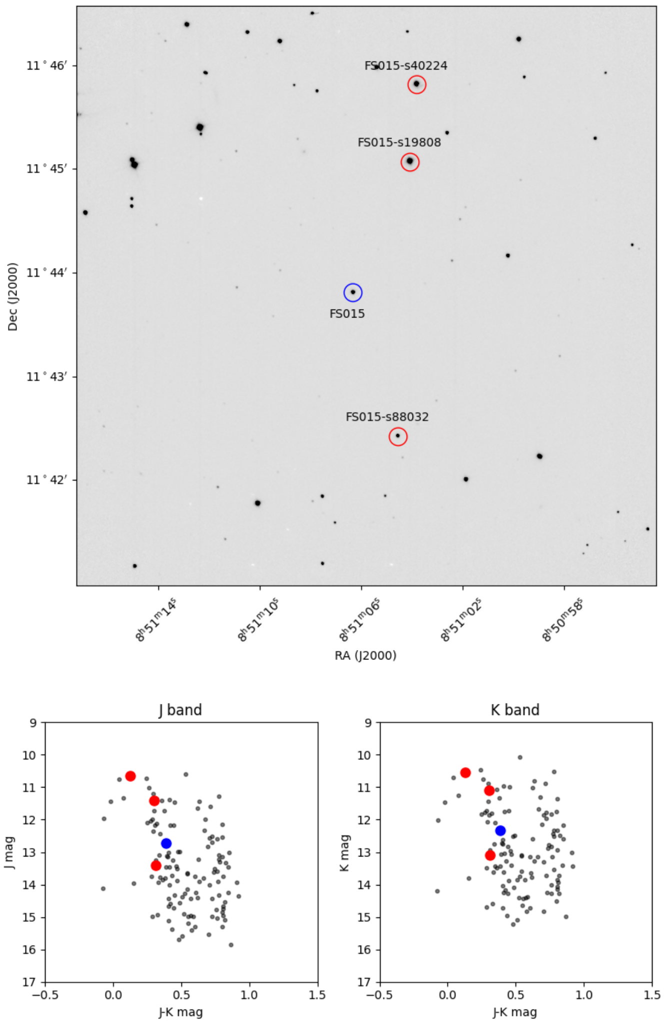

Figure 12. FS015 field finding chart and color-magnitude diagrams

Table 8. FS015

name	ra	dec	J	err J	epochs J	K	err K	epochs K	GAIA id
FS015-s19808	8:51:03.51	11:45:02.82	10.658	0.008	6	10.530	0.005	6	604911135364519808
FS015-s40224	8:51:03.26	11:45:47.41	11.409	0.008	5	11.105	0.003	5	604914468259140224
FS015	8:51:05.76	11:43:46.97	12.722	0.010	6	12.336	0.008	6	604910860486613632
FS015-s88032	8:51:03.99	11:42:23.95	13.408	0.010	6	13.097	0.007	6	604910654328188032

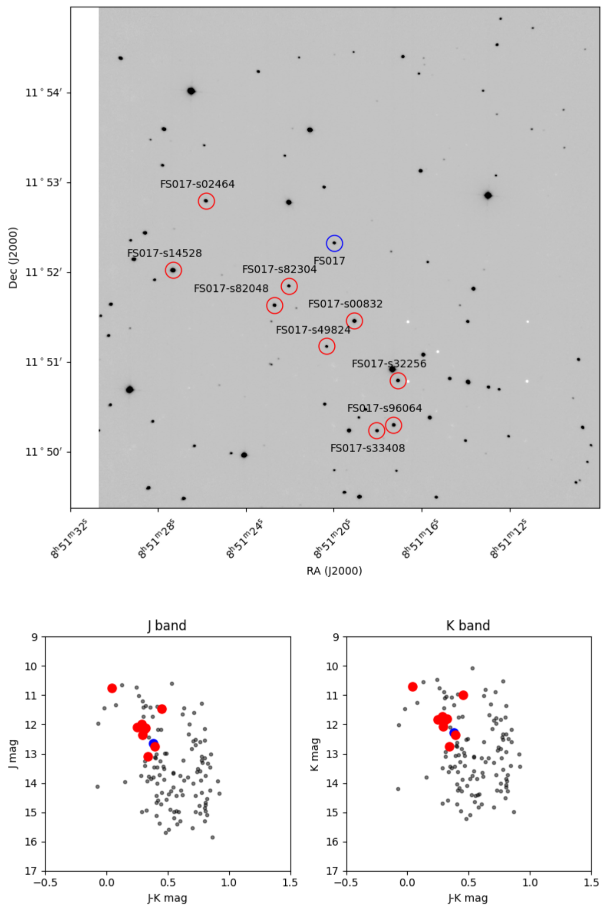

Figure 13. FS017 field finding chart and color-magnitude diagrams

Table 9. FS017

name	ra	dec	J	err J	epochs J	K	err K	epochs K	GAIA id
FS017-s14528	8:51:27.01	11:51:52.58	10.742	0.009	7	10.699	0.005	7	604921202767814528
FS017-s00832	8:51:18.77	11:51:18.71	11.455	0.008	7	11.001	0.003	7	604921129752600832
FS017-s32256	8:51:16.79	11:50:39.02	12.000	0.011	7	11.714	0.006	7	604920756091232256
FS017-s96064	8:51:16.98	11:50:09.44	12.083	0.009	7	11.835	0.005	7	604920721731496064
FS017-s02464	8:51:25.52	11:52:38.83	12.117	0.010	7	11.797	0.007	7	604921271487102464
FS017-s82048	8:51:22.41	11:51:29.24	12.170	0.008	7	11.864	0.003	7	604921168408082048
FS017-s33408	8:51:17.75	11:50:05.60	12.357	0.010	7	12.065	0.006	7	604920756091233408
FS017	8:51:19.69	11:52:10.75	12.655	0.009	7	12.273	0.005	7	604921374566324992
FS017-s82304	8:51:21.76	11:51:42.06	12.760	0.010	7	12.368	0.004	7	604921168408082304
FS017-s49824	8:51:20.04	11:51:01.70	13.084	0.009	7	12.744	0.006	7	604921134048349824

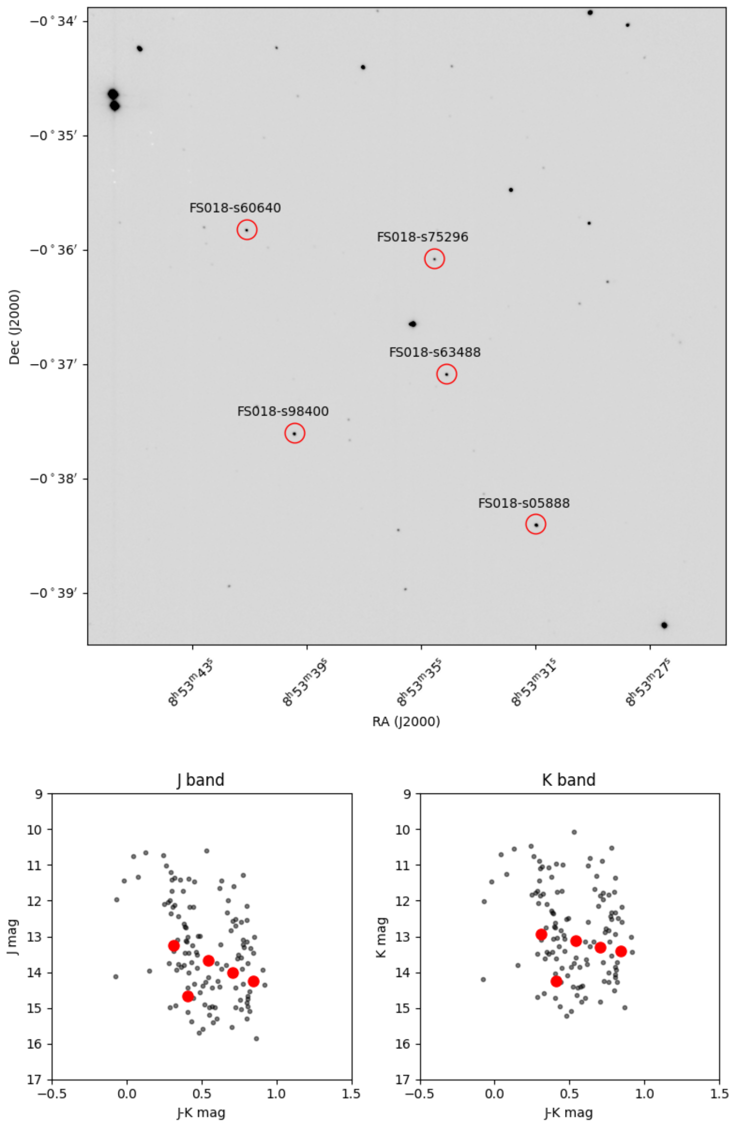

Figure 14. FS018 field finding chart and color-magnitude diagrams

Table 10. FS018

name	ra	dec	J	err J	epochs J	K	err K	epochs K	GAIA id
FS018-s05888	8:53:31.19	-0:38:26.70	13.247	0.007	8	12.934	0.004	8	3074350479674405888
FS018-s98400	8:53:39.64	-0:37:38.82	13.659	0.010	8	13.116	0.009	8	3074350926350998400
FS018-s63488	8:53:34.29	-0:37:07.72	14.000	0.005	8	13.292	0.006	8	3074350891991263488
FS018-s60640	8:53:41.35	-0:35:51.76	14.260	0.010	8	13.416	0.006	8	3074352506898960640
FS018-s75296	8:53:34.75	-0:36:07.33	14.669	0.010	8	14.260	0.008	8	3074353950007975296

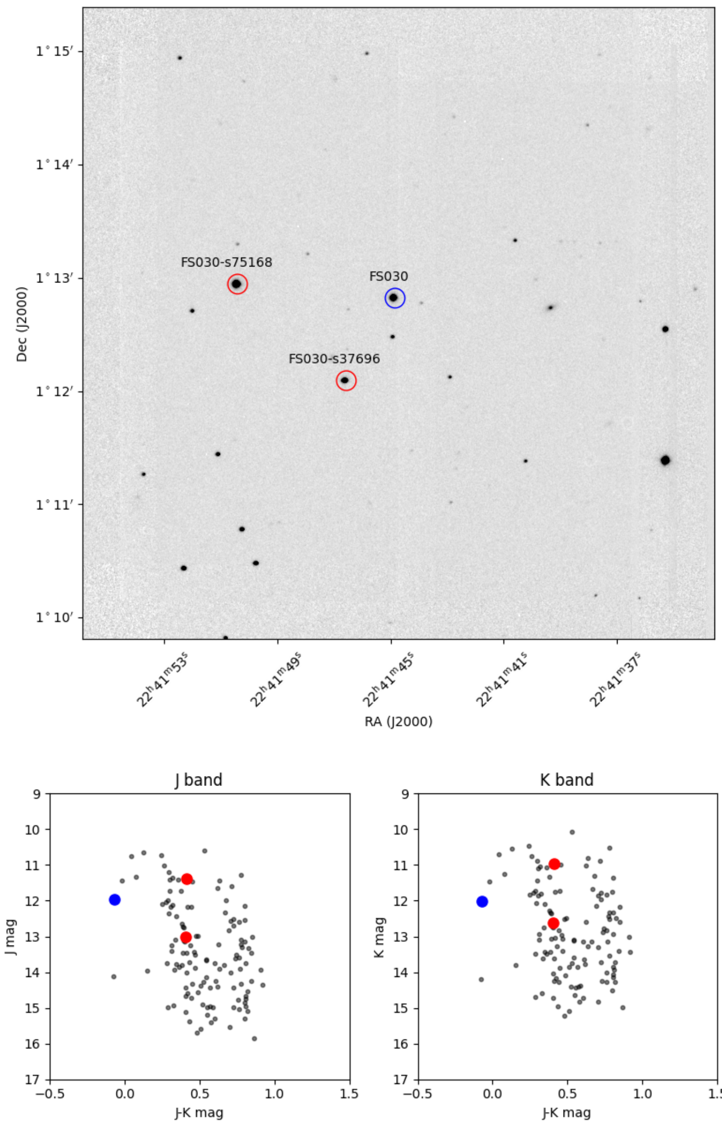

Figure 15. FS030 field finding chart and color-magnitude diagrams

Table 11. FS030

name	ra	dec	J	err J	epochs J	K	err K	epochs K	GAIA id
FS030-s75168	22:41:50.24	1:12:43.25	11.383	0.011	6	10.972	0.007	6	2654543123279175168
FS030	22:41:44.70	1:12:36.37	11.949	0.008	6	12.018	0.008	6	2654543161934285440
FS030-s37696	22:41:46.40	1:11:52.20	13.018	0.007	6	12.613	0.004	6	2654543088919437696

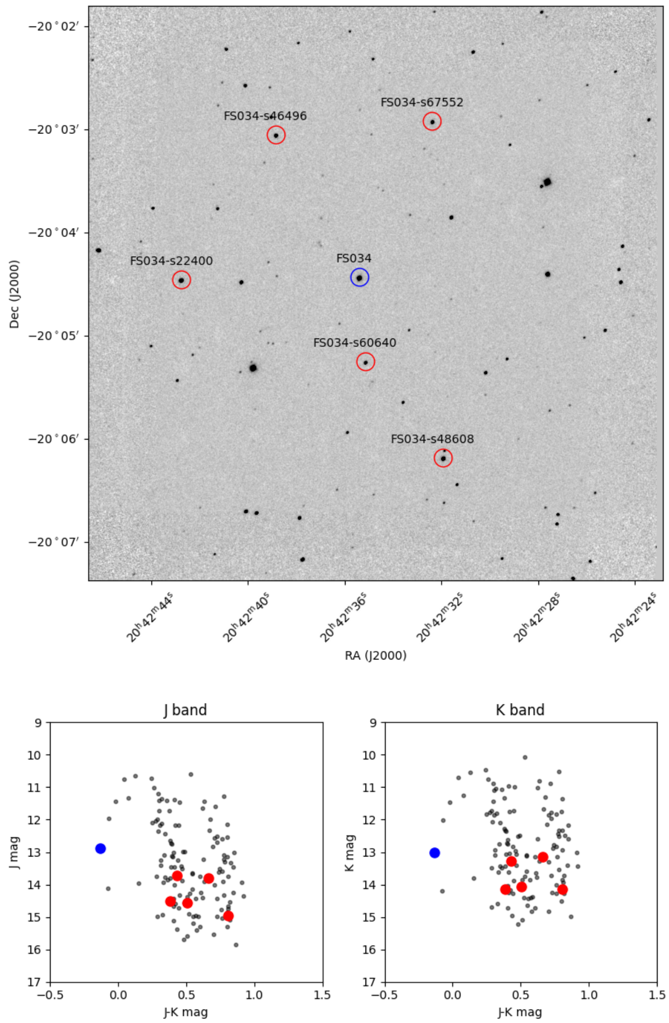

Figure 16. FS034 field finding chart and color-magnitude diagrams

Table 12. FS034

name	ra	dec	J	err J	epochs J	K	err K	epochs K	GAIA id
FS034	20:42:34.75	-20:04:35.93	12.872	0.009	11	13.000	0.009	11	6857939315643803776
FS034-s22400	20:42:42.43	-20:04:38.54	13.715	0.010	9	13.285	0.009	9	6857939624881622400
FS034-s48608	20:42:31.61	-20:06:22.27	13.812	0.009	11	13.149	0.008	11	6857939109486948608
FS034-s46496	20:42:38.52	-20:03:14.20	14.561	0.006	11	14.056	0.006	11	6857942682898346496
FS034-s60640	20:42:34.81	-20:05:26.37	14.948	0.009	10	14.140	0.008	10	6857939208267760640

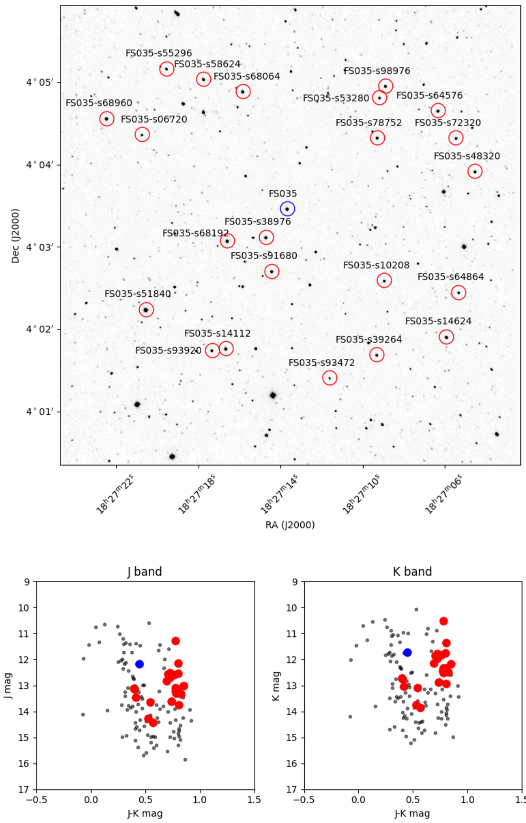

Figure 17. FS035 field finding chart and color-magnitude diagrams

Table 13. FS035

name	ra	dec	J	err J	epochs J	K	err K	epochs K	GAIA id
FS035-s51840	18:27:20.35	4:01:56.29	11.289	0.007	6	10.511	0.008	6	4284122439177651840
FS035-s68192	18:27:16.40	4:02:46.41	12.147	0.008	6	11.344	0.011	6	4284122709739768192
FS035	18:27:13.50	4:03:09.80	12.182	0.007	6	11.734	0.009	6	4284122748415319936
FS035-s14112	18:27:16.46	4:01:27.90	12.513	0.008	6	11.788	0.011	6	4284122370460714112
FS035-s68960	18:27:22.27	4:04:15.46	12.550	0.008	6	11.749	0.011	6	4284128623930568960
FS035-s68064	18:27:15.64	4:04:35.09	12.555	0.008	6	11.847	0.009	6	4284129414204568064
FS035-s38976	18:27:14.54	4:02:49.07	12.604	0.008	6	11.841	0.010	6	4284122679695838976
FS035-s14624	18:27:05.74	4:01:36.46	12.686	0.007	6	11.960	0.011	6	4284122610975914624
FS035-s91680	18:27:14.23	4:02:24.39	12.830	0.008	6	12.135	0.010	6	4284122675379991680
FS035-s58624	18:27:17.55	4:04:44.10	13.023	0.008	6	12.171	0.010	6	4284128692650058624
FS035-s48320	18:27:04.34	4:03:36.90	13.097	0.006	6	12.317	0.010	6	4284123469969848320
FS035-s78752	18:27:09.10	4:04:01.43	13.120	0.008	6	12.723	0.011	6	4284123504329578752
FS035-s93920	18:27:17.15	4:01:26.72	13.143	0.008	6	12.340	0.010	6	4284122473537393920
FS035-s64576	18:27:06.15	4:04:20.90	13.144	0.007	6	12.742	0.010	6	4284123573049064576
FS035-s98976	18:27:08.70	4:04:39.06	13.222	0.008	6	12.446	0.011	6	4284123607408798976
FS035-s39264	18:27:09.13	4:01:23.48	13.290	0.009	6	12.507	0.009	6	4284122537940939264
FS035-s72320	18:27:05.27	4:04:01.24	13.322	0.007	6	12.498	0.009	6	4284123573049272320
FS035-s10208	18:27:08.75	4:02:17.38	13.456	0.007	6	13.040	0.010	6	4284122645336110208
FS035-s64864	18:27:05.15	4:02:08.85	13.610	0.009	6	12.872	0.011	6	4284123366890164864
FS035-s53280	18:27:08.99	4:04:30.61	13.638	0.007	6	13.094	0.010	6	4284123603093153280
FS035-s55296	18:27:19.35	4:04:51.71	13.749	0.008	6	12.941	0.009	6	4284128692650055296
FS035-s06720	18:27:20.54	4:04:03.76	14.264	0.008	6	13.737	0.009	6	4284128623920206720
FS035-s93472	18:27:11.41	4:01:06.61	14.424	0.007	6	13.856	0.007	6	4284122336097993472

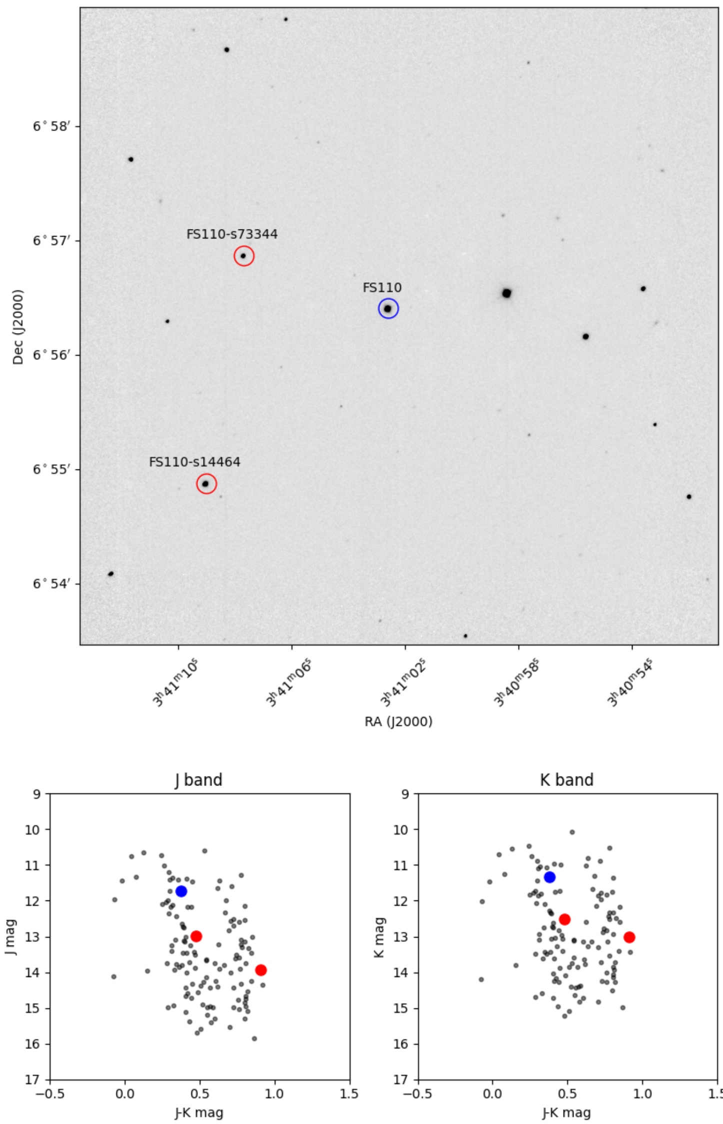

Figure 18. FS110 field finding chart and color-magnitude diagrams

Table 14. FS110

name	ra	dec	J	err J	epochs J	K	err K	epochs K	GAIA id
FS110	3:41:02.22	6:56:16.43	11.715	0.007	11	11.336	0.004	11	3277706323464131968
FS110-s14464	3:41:08.64	6:54:44.94	12.990	0.010	11	12.512	0.006	11	3277659113183614464
FS110-s73344	3:41:07.29	6:56:44.49	13.928	0.006	11	13.018	0.003	11	3277659525500473344

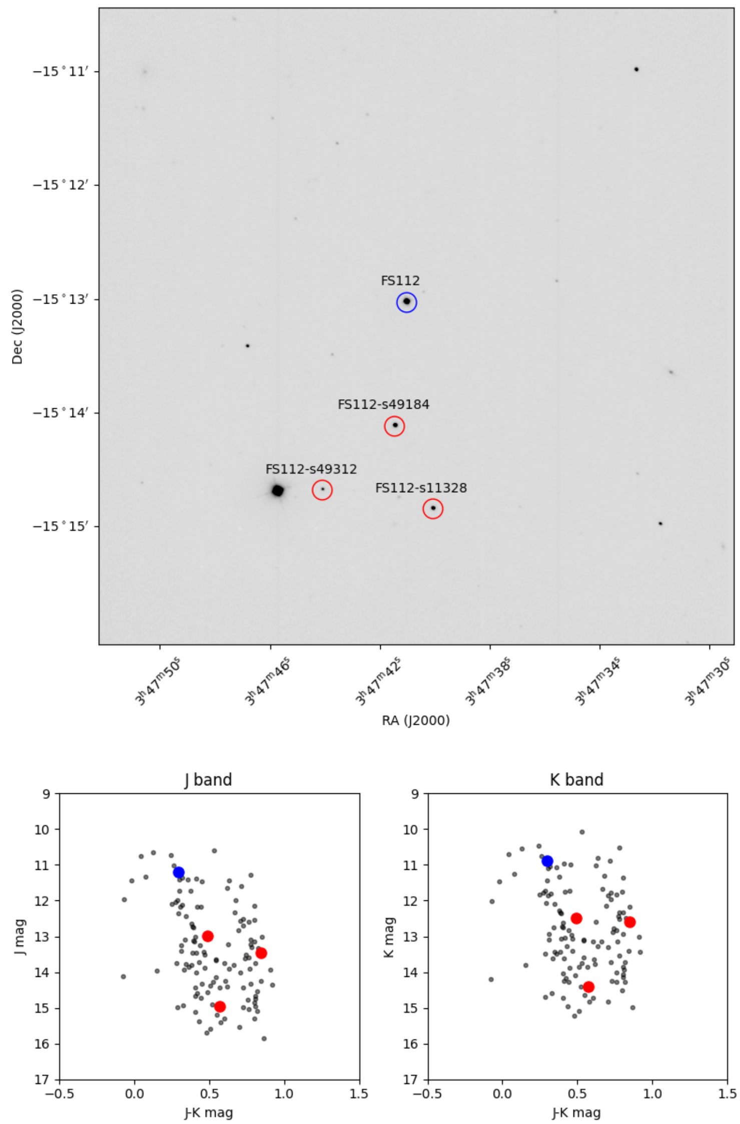

Figure 19. FS112 field finding chart and color-magnitude diagrams

Table 15. FS112

name	ra	dec	J	err J	epochs J	K	err K	epochs K	GAIA id
FS112	3:47:40.72	-15:13:14.59	11.190	0.007	10	10.893	0.005	10	5109048973678255488
FS112-s49184	3:47:41.12	-15:14:19.76	12.980	0.009	10	12.490	0.004	10	5109048698800349184
FS112-s11328	3:47:39.72	-15:15:03.20	13.447	0.008	10	12.600	0.004	10	5109048664440611328
FS112-s49312	3:47:43.76	-15:14:53.51	14.966	0.010	10	14.393	0.006	10	5109048698800349312

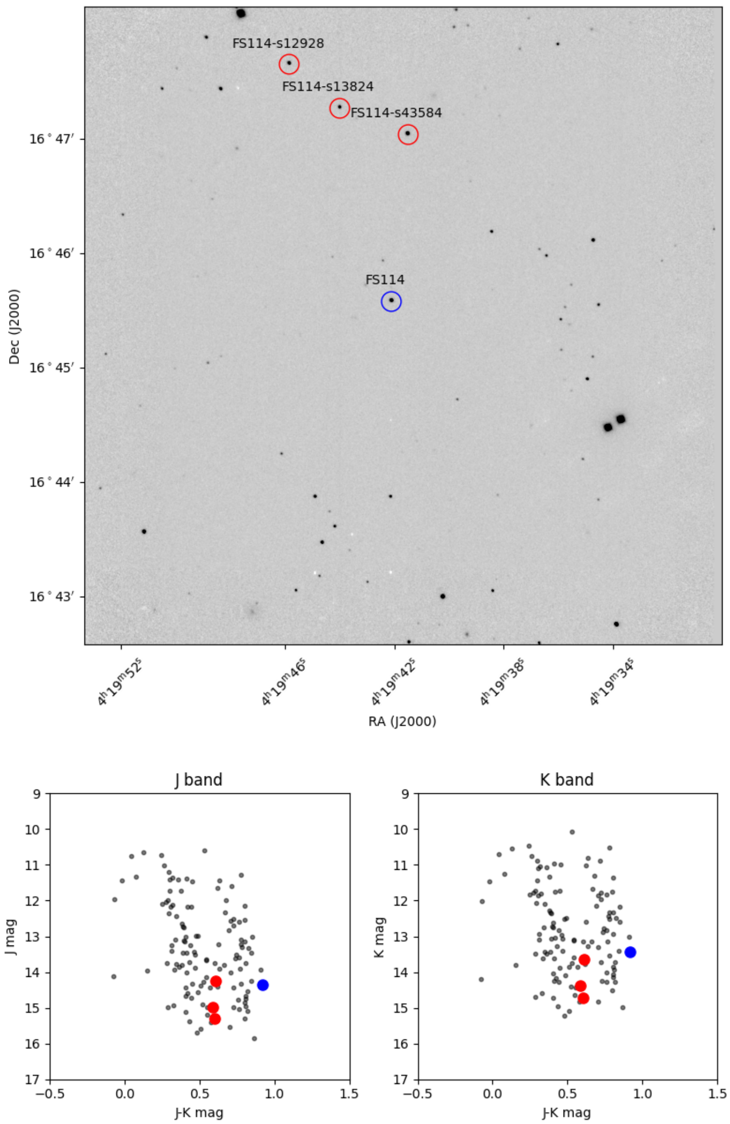

Figure 20. FS114 field finding chart and color-magnitude diagrams

Table 16. FS114

name	ra	dec	J	err J	epochs J	K	err K	epochs K	GAIA id
FS114-s43584	4:19:41.20	16:46:48.45	14.246	0.006	23	13.635	0.004	23	3313880805773043584
FS114	4:19:41.73	16:45:22.05	14.360	0.004	26	13.442	0.003	26	3313879946778443648
FS114-s12928	4:19:45.53	16:47:25.32	14.981	0.008	17	14.392	0.010	17	3313880152938012928
FS114-s13824	4:19:43.68	16:47:02.19	15.311	0.006	22	14.708	0.009	22	3313880152938013824

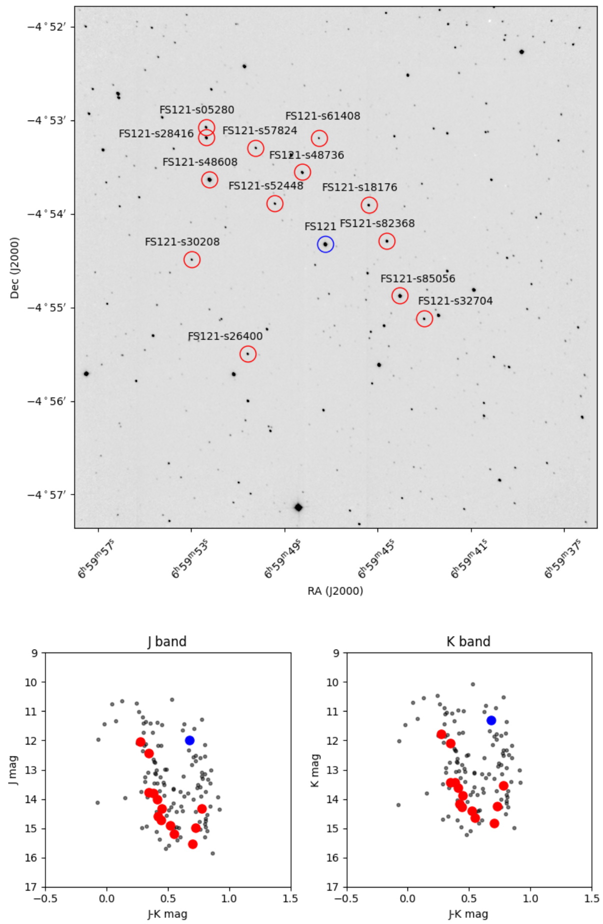

Figure 21. FS121 field finding chart and color-magnitude diagrams

Table 17. FS121

name	ra	dec	J	err J	epochs J	K	err K	epochs K	GAIA id
FS121	6:59:46.77	-4:54:33.67	11.977	0.003	16	11.300	0.003	16	3101625583593341568
FS121-s48608	6:59:51.74	-4:53:52.27	12.051	0.006	16	11.775	0.006	16	3101625686672548608
FS121-s85056	6:59:43.57	-4:55:06.81	12.434	0.006	16	12.087	0.005	16	3101625617953085056
FS121-s28416	6:59:51.88	-4:53:25.54	13.777	0.007	16	13.429	0.009	16	3101625716732828416
FS121-s82368	6:59:44.13	-4:54:31.69	13.811	0.004	16	13.426	0.005	16	3101625617953082368
FS121-s48736	6:59:47.77	-4:53:47.64	14.015	0.005	16	13.604	0.006	16	3101625751092548736
FS121-s18176	6:59:44.92	-4:54:08.63	14.323	0.005	16	13.543	0.006	16	3101625652312818176
FS121-s05280	6:59:51.89	-4:53:18.68	14.328	0.009	16	13.877	0.009	16	3101625785452305280
FS121-s32704	6:59:42.54	-4:55:21.41	14.581	0.006	16	14.159	0.006	16	3101602145952232704
FS121-s26400	6:59:50.11	-4:55:43.84	14.721	0.008	16	14.277	0.005	16	3101613793903526400
FS121-s52448	6:59:48.94	-4:54:07.64	14.917	0.004	16	14.396	0.009	16	3101625686672552448
FS121-s57824	6:59:49.76	-4:53:32.07	14.986	0.007	16	14.259	0.009	16	3101625751092557824
FS121-s30208	6:59:52.50	-4:54:43.50	15.184	0.005	16	14.633	0.009	16	3101613935642030208
FS121-s61408	6:59:47.05	-4:53:25.76	15.538	0.007	16	14.835	0.011	16	3101625751092561408

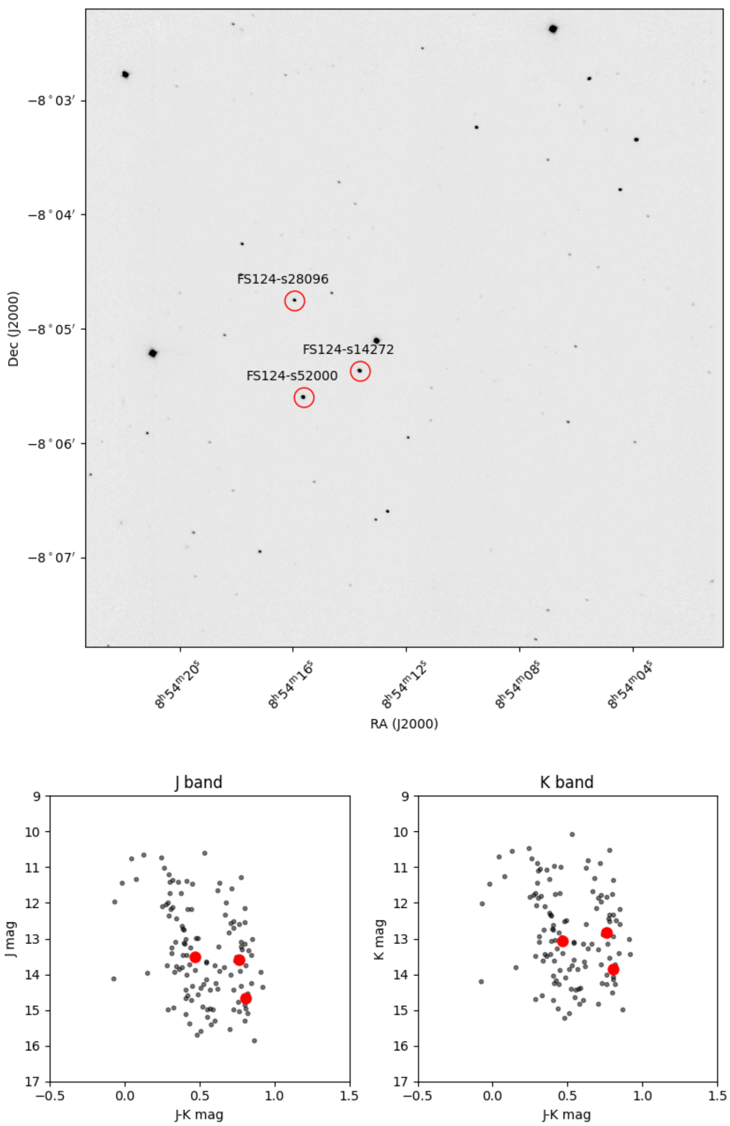

Figure 22. FS124 field finding chart and color-magnitude diagrams

Table 18. FS124

name	ra	dec	J	err J	epochs J	K	err K	epochs K	GAIA id
FS124-s14272	8:54:13.83	-8:05:27.00	13.524	0.007	14	13.056	0.005	14	5756746672027014272
FS124-s52000	8:54:15.83	-8:05:41.04	13.584	0.008	14	12.820	0.005	14	5756746706386752000
FS124-s28096	8:54:16.12	-8:04:49.83	14.666	0.005	14	13.860	0.004	14	5756746775106228096

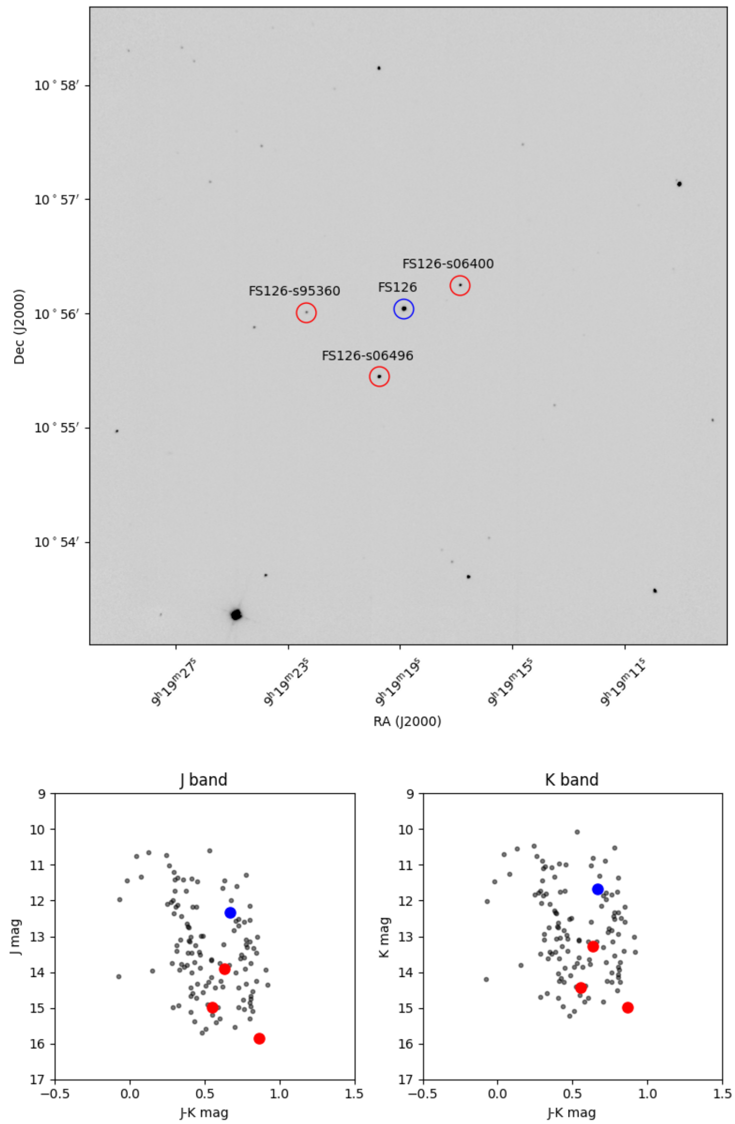

Figure 23. FS126 field finding chart and color-magnitude diagrams

Table 19. FS126

name	ra	dec	J	err J	epochs J	K	err K	epochs K	GAIA id
FS126	9:19:18.75	10:55:51.10	12.330	0.009	9	11.662	0.006	9	592615193750958464
FS126-s06496	9:19:19.62	10:55:15.38	13.901	0.004	9	13.268	0.005	9	592615086376506496
FS126-s06400	9:19:16.73	10:56:03.41	14.993	0.011	9	14.441	0.009	9	592615258175206400
FS126-s95360	9:19:22.20	10:55:49.09	15.854	0.010	9	14.988	0.010	9	592615193751295360

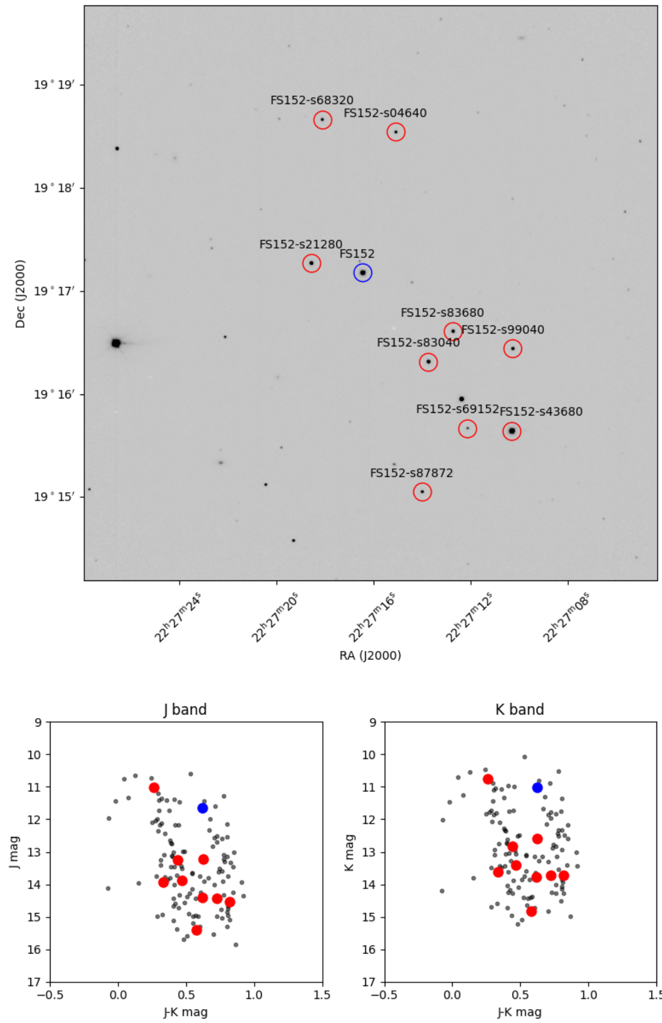

Figure 24. FS152 field finding chart and color-magnitude diagrams

Table 20. FS152

name	ra	dec	J	err J	epochs J	K	err K	epochs K	GAIA id
FS152-s43680	22:27:10.01	19:15:23.11	11.017	0.006	11	10.756	0.006	11	1777401846705943680
FS152	22:27:16.14	19:16:55.41	11.639	0.004	11	11.017	0.007	11	1777402018504634496
FS152-s21280	22:27:18.26	19:17:00.86	13.218	0.005	11	12.592	0.008	11	1777402022799921280
FS152-s83040	22:27:13.43	19:16:03.40	13.262	0.005	11	12.820	0.008	11	1777401988440183040
FS152-s83680	22:27:12.41	19:16:21.06	13.872	0.004	11	13.404	0.005	11	1777401988440183680
FS152-s99040	22:27:09.95	19:16:11.06	13.945	0.008	11	13.610	0.007	11	1777402091519399040
FS152-s87872	22:27:13.69	19:14:47.74	14.395	0.010	11	13.776	0.011	11	1777401816641487872
FS152-s68320	22:27:17.80	19:18:24.51	14.442	0.005	11	13.718	0.007	11	1777403702132168320
FS152-s04640	22:27:14.77	19:18:17.29	14.531	0.006	11	13.713	0.006	11	1777403706427104640
FS152-s69152	22:27:11.83	19:15:24.69	15.392	0.009	11	14.814	0.009	11	1777401881065969152

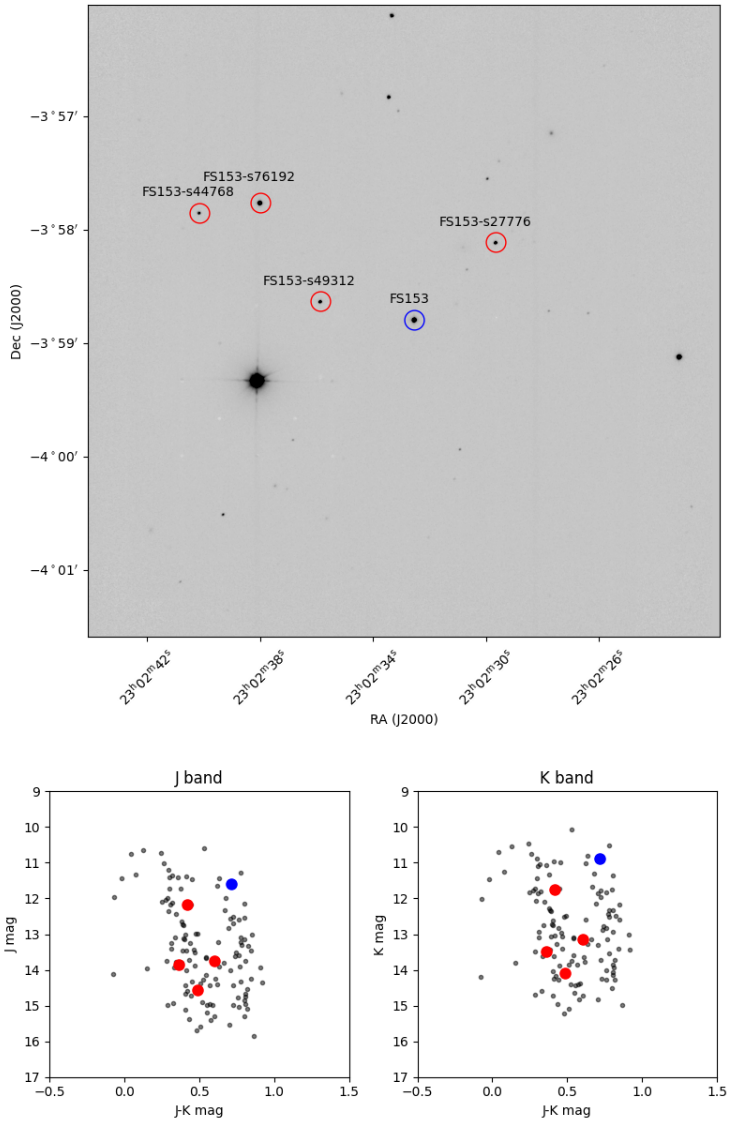

Figure 25. FS153 field finding chart and color-magnitude diagrams

Table 21. FS153

name	ra	dec	J	err J	epochs J	K	err K	epochs K	GAIA id
FS153	23:02:32.08	-3:58:53.03	11.590	0.005	0.009	10.874	0.006	0.010	2636398540016611200
FS153-s76192	23:02:37.53	-3:57:51.46	12.180	0.006	0.012	11.763	0.006	0.009	2636398677455576192
FS153-s49312	23:02:35.40	-3:58:43.55	13.740	0.005	0.006	13.137	0.006	0.013	2636398574376349312
FS153-s27776	23:02:29.20	-3:58:12.29	13.841	0.008	0.022	13.480	0.008	0.024	2636398604440827776
FS153-s44768	23:02:39.68	-3:57:56.67	14.566	0.006	0.016	14.079	0.009	0.030	2636395752582544768

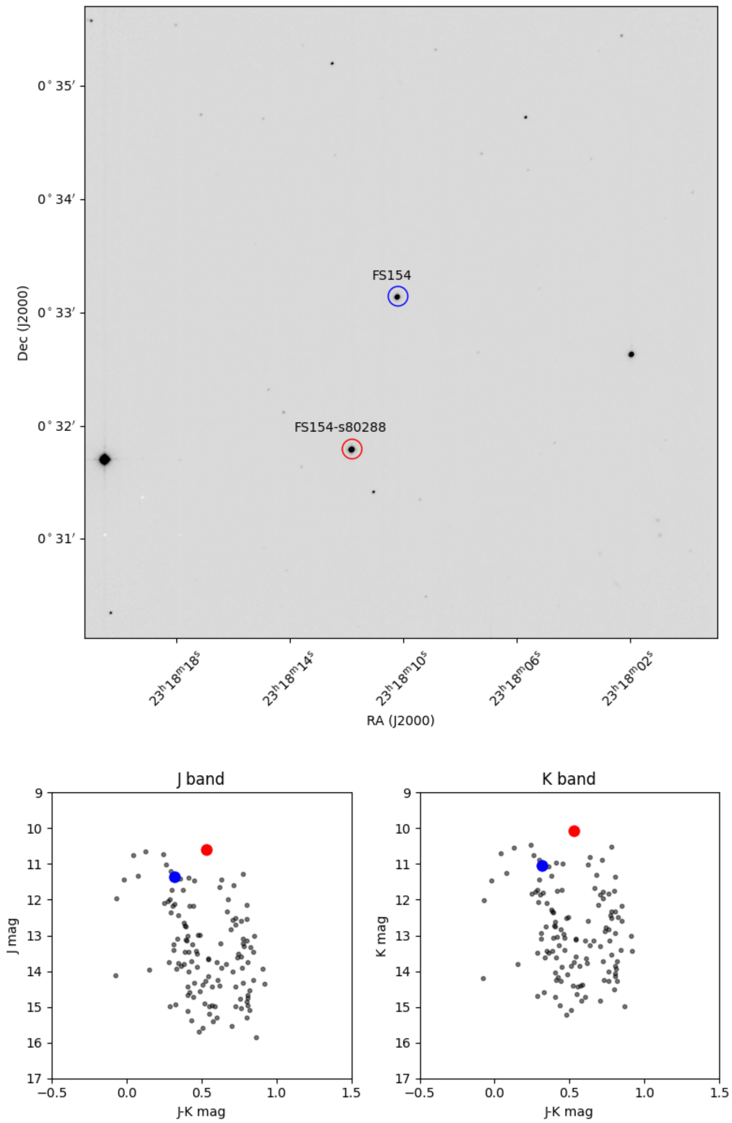

Figure 26. FS154 field finding chart and color-magnitude diagrams

Table 22. FS154

name	ra	dec	J	err J	epochs J	K	err K	epochs K	GAIA id
FS154-s80288	23:18:11.63	0:31:35.57	10.597	0.006	9	10.065	0.010	9	2645250501973180288
FS154	23:18:10.02	0:32:56.09	11.356	0.003	9	11.038	0.004	9	2645253559989894912